Novel insights into deep groundwater exploration by geophysical estimation of hard rock permeability

Muhammad Hasan [1, 2, 3,*], **Lijun Su** [1, 2, 3, **]

[1] *State Key Laboratory of Mountain Hazards and Engineering Resilience, Institute of Mountain Hazards and Environment, Chinese Academy of Sciences, Chengdu 610299, China*

[2] *China-Pakistan Joint Research Center on Earth Sciences, CAS-HEC, Islamabad, Pakistan*

[3] *University of Chinese Academy of Sciences, Beijing 100049, China*

*Corresponding authors:

Muhammad Hasan: Email: mhasan@imde.ac.cn; ORCID: https://orcid.org/0000-0001-6804-7962; Phone Number: +86-13051361710

Lijun Su: Email: sulijun1976@163.com; ORCID: https://orcid.org/0000-0001-9972-4698

Corresponding authors' postal address: State Key Laboratory of Mountain Hazards and Engineering Resilience, Institute of Mountain Hazards and Environment, Chinese Academy of Sciences, Chengdu 610299, China

Abstract

Deep groundwater exploration in hard rock terrains is critical in regions where deep aquifers may offer long-term water security amidst increasing scarcity. However, such exploration is globally challenged by geological complexity and the limitations of traditional investigative techniques. Accurate estimation of hydraulic parameters, particularly permeability (*k*), is essential for effective groundwater management and future resource planning. Conventional borehole-based methods for measuring *k* are invasive, costly, time-consuming, and limited to sparse, point-scale observations, making them inadequate for characterizing deep and heterogeneous aquifer systems. Geophysical methods offer a promising non-invasive alternative, enabling broader spatial coverage with reduced surface disturbance. While previous studies have used empirical approaches, such as vertical electrical sounding (VES), to estimate *k*, these techniques are typically constrained to shallow depths (typically <200 m), homogeneous conditions, and one-dimensional interpretations. This study advances the application of resistivity-based geophysical methods by demonstrating, for the first time, the use of controlled-source audio-frequency magnetotellurics (CSAMT) to estimate two- and three-dimensional *k* distributions to depths exceeding 1 km across complex geological settings, including sedimentary, igneous, and metamorphic formations. In doing so, it extends the scope of earlier hydrogeophysical research, which has largely focused on shallower or more uniform subsurface environments. The results show that, when calibrated with borehole data, CSAMT can reliably capture deep subsurface variability and produce spatially continuous hydrogeological models in hard rock terrains, particularly in areas with limited borehole coverage. While CSAMT inversion is inherently ill-posed, the incorporation of ground-truth data significantly enhances model robustness and interpretability. This integrated approach reduces dependence on extensive borehole drilling and

enables broader and more economical evaluation of aquifer potential. The methodology represents a significant advancement in deep groundwater exploration and offers valuable insights for sustainable groundwater resource management and long-term water security in geologically complex hard rock regions.

Keywords: Permeability; Geophysical methods; Hydraulic parameters; Groundwater; Hard rock; Hydrogeological models

1 Introduction

Metamorphic and igneous rocks dominate Earth's crust and cover about one-third of its surface (Amiotte Suchet et al., 2003). In hard rock terrains, groundwater research focuses on delineating subsurface structures, such as faults and fractures that control water storage and flow (Fernando and Pacheco, 2015; Hasan et al., 2021). A key parameter in this context is aquifer potential, which reflects the capacity of rock formations to store and transmit groundwater and is influenced by lithology, structural complexity, mineral composition, weathering, and infiltration depth (Majumdar and Das, 2011; Zhu et al., 2017). However, accurately characterizing the lateral and vertical heterogeneity of these properties remains challenging due to limited data and the complexity of massive rock units (Dewandel et al., 2006). In such settings, conventional methods often fall short, leading to inefficient or unsustainable groundwater development (Nwosu et al., 2013; Worthington et al., 2016). Developing cost-effective and reliable approaches for subsurface assessment is therefore essential for managing groundwater in hard rock environments.

Groundwater at depths beyond 500 m is typically isolated from surface hydrological influences and often exhibits brackish or saline characteristics (Ferguson et al., 2023). Its

strategic importance is increasingly recognized, particularly in geologically and environmentally constrained settings (Gleeson et al., 2014). In the Jinji region, several factors necessitate focused investigation of deep aquifers. Surface water is scarce and unreliable, while the shallow subsurface is dominated by fresh granite, which has inherently low porosity and permeability, limiting groundwater availability. By contrast, deeper fractured zones in granite, sandstone, and hornstone present more favorable hydrogeological conditions. Recent national water initiatives in China have emphasized deep subsurface exploration in structurally complex terrains to identify underutilized aquifers for enhancing long-term water security. Comprehensive assessment of these deep reserves is essential to evaluate their recharge potential and integrate them into sustainable resource management strategies (Condon et al., 2020; Hasan and Shang, 2022). As pressure on surface and shallow groundwater intensifies, deep aquifers may serve as a vital buffer against increasing environmental and socio-economic stress.

Multiple studies have documented the rapid depletion of global groundwater reserves, raising serious concerns about long-term water sustainability (Wada et al., 2010; Laghari et al., 2012; Jasechko et al., 2024). Addressing this challenge requires accurate and detailed assessments of groundwater resources, which depend critically on a clear understanding of subsurface hydraulic properties. Permeability (k) is a key parameter that describes the ease with which fluids can move through a porous medium, while the capacity to store water is more directly characterized by porosity. This parameter is crucial for aquifer analysis in various hydrogeological settings (Allègre et al., 2016; Esmaeilpour et al., 2023; Carbillet et al., 2024). Borehole testing remains the standard method for estimating k and related aquifer parameters (De Lima and Niwas, 2000; Hasan et al., 2021). However, borehole investigations are often limited by high costs, logistical challenges, and poor spatial coverage, particularly in rugged

terrains, while offering only localized information with limited ability to image lateral and deep structures (Singh, 2005; Fiandaca et al., 2018). These limitations contribute to uncertainties in groundwater assessments, especially in data-scarce regions (Hasan and Shang, 2022). Alternatively, it is essential to develop methods that minimize reliance on costly drilling while still enabling reliable estimation of permeability within prospective rock formations.

Geophysical methods are widely and effectively employed to enhance subsurface characterization in groundwater studies (Daily et al., 1992; Jardani et al., 2007; Hinnell et al., 2010; Fu et al., 2013; Jiang et al., 2014; Kouadio et al., 2023). Compared to conventional drilling, these techniques offer significant advantages in cost, deployment speed, environmental impact, and spatial extent (Hu et al., 2013; Fusheng et al., 2022). Their ability to image both vertical and lateral subsurface variations makes them particularly effective in heterogeneous terrains (Hasan et al., 2025). Among them, resistivity-based methods are widely used due to their sensitivity to lithology, porosity, fractures, and fluid content (Hasan et al., 2021; Asfahani, 2023). Common techniques include electrical resistivity tomography (ERT), vertical electrical sounding (VES), and electromagnetic methods such as magnetotellurics (MT), time-domain electromagnetics (TDEM), and controlled-source audio-frequency magnetotellurics (CSAMT) (Soupios et al., 2007; Bauer-Gottwein et al., 2010; Pollock and Cirpka, 2012; Jiang et al., 2014; Di et al., 2020). VES offers a budget-friendly solution for shallow 1D (one-dimensional) profiling (typically <200 m) but lacks lateral resolution in complex settings (Niwas and De Lima, 2003; Majumdar and Das, 2011). ERT offers improved 2D (two-dimensional) and 3D (three-dimensional) imaging up to ~300 m depth, making it suitable for fractured and karst systems; though it requires more field effort and is less effective in extreme resistivity conditions (Abbas et al., 2022; Hasan and Shang, 2022). For deeper targets, electromagnetic methods such as

TDEM, MT, and CSAMT are often employed (Bauer-Gottwein et al., 2010; Di et al., 2020; Gonzalez-Duque et al., 2024). MT provides excellent depth penetration (up to tens of kilometers) and is widely used in regional-scale studies and geothermal exploration, though it requires long acquisition times and is sensitive to cultural noise (Simpson and Bahr, 2005). TDEM offers a compromise between resolution and depth, reaching several hundred meters with rapid deployment, but can be constrained by near-surface conductivity and limited sensitivity at greater depths (Bauer-Gottwein et al., 2010). CSAMT, by contrast, bridges the gap between these methods. With controlled-source signals and frequency tuning, CSAMT enables high-resolution 2D and 3D imaging of conductive structures over 1,000 m depth, even in culturally noisy and geologically complex settings (Smith and Booker, 1991; Zhang et al., 2021). Although its spatial resolution is generally lower than ERT, CSAMT offers superior performance for deep hydrogeological investigations, especially when integrated with borehole data and empirical modeling (Zonge and Hughes, 1991; Wang et al., 2015). The choice between resistivity and electromagnetic techniques is contingent upon parameters like investigation depth, resolution requirements, geological complexity, and logistical constraints (Majumdar and Das, 2011; Hasan et al., 2025). Given the objectives of this study, to delineate deep aquifer structures in a hard rock setting, CSAMT was selected as the most suitable method, offering a practical balance of depth penetration, imaging capability, and field adaptability.

In fractured rocks like granite, metamorphic, and sandstone formations, fluid flow is largely controlled by fracture networks rather than matrix porosity. Accurate hydraulic assessment in such settings benefits from integrated geophysical and hydrogeological approaches to better capture spatial variability and improve flow modeling (Hasan et al., 2021; Abbas et al., 2022). Resistivity-based techniques are particularly valuable for delineating subsurface structures

and identifying water-bearing zones. Because electrical resistivity is sensitive to porosity, saturation, fracture density, and fluid salinity, it is increasingly used to infer *k* in heterogeneous geological settings (Mudunuru et al., 2022; Yan et al., 2024). Permeability is influenced by numerous parameters, including porosity, fracture density and orientation, grain size distribution, degree of weathering, pore connectivity, and saturation level, highlighting the utility of resistivity measurements as indicators for evaluating groundwater flow potential (Gerke et al., 2011; Worthington et al., 2016; Pellet et al., 2024).

Empirical and semi-empirical models have been developed to estimate hydraulic properties from geophysical measurements, particularly in data-sparse regions (Niwas and De Lima, 2003; Singh, 2005; Soupios et al., 2007; Hasan et al., 2021; Asfahani, 2023). In parallel, resistivity-based methods and hydrogeophysical inversion techniques have been developed to more rigorously estimate hydraulic parameters by integrating petrophysical relationships within geophysical modeling frameworks (Daily et al., 1992; Ferré et al., 2009; Binley et al., 2010; Hinnell et al., 2010; Herckenrath et al., 2012; Pollock and Cirpka, 2012; Herckenrath et al., 2013; Binley et al., 2015). These approaches have improved resolution in parameter estimation, particularly in shallow, unconsolidated, or relatively homogeneous settings. However, applications to deep, fractured, and lithologically complex environments remain limited, especially in terms of producing volumetric *k* models at kilometer-scale depths. Despite these advances, generation of detailed 2D and 3D *k* maps from resistivity data in deep, hard-rock terrains is constrained by limited borehole control, significant geological heterogeneity, and the ill-posed nature of geophysical inversion. In such contexts, integrating resistivity data with borehole measurements presents a practical, cost-effective solution for characterizing aquifer properties over large areas and depth ranges. This study builds on prior hydrogeophysical

research and introduces a novel application of the CSAMT method for volumetric *k* modeling in a complex, fractured hard-rock setting. While previous studies have applied resistivity-based techniques to estimate hydraulic properties, this is the first to utilize CSAMT for constructing the detailed 2D and 3D *k* modeling beyond 1000 m depth in geologically heterogeneous terrains comprising hornstone, granite, and sandstone. Few available drilling tests were used to calibrate CSAMT-derived resistivity with laboratory-measured *k*, allowing the resulting empirical relationship to be applied across the broader survey domain. Several CSAMT profiles were conducted along and beyond the borehole locations, and the calibrated resistivity–permeability correlation was used to generate spatially continuous subsurface models in regions lacking direct borehole data. This integration resulted in a robust, data-constrained workflow capable of revealing *k* variations across diverse rock units and lithological boundaries. The method offers a practical and scalable alternative to extensive drilling campaigns, enabling a more detailed and cost-efficient evaluation of deep groundwater potential in structurally complex terrains.

Ultimately, this work extends the scope of hydrogeophysical methods by demonstrating the feasibility of applying CSAMT for deep hydraulic parameter estimation in hard rock. It bridges a critical methodological gap in hard-rock hydrogeology and sets the foundation for future CSAMT-based volumetric modeling in similarly challenging environments. This study aims to develop and apply a geophysical-based approach for mapping the spatial distribution of *k* in deep, hard-rock settings. By integrating CSAMT data with targeted borehole measurements, this research enhances 2D and 3D hydrogeological assessments across heterogeneous lithologies in structurally complex terrains. It also minimizes reliance on extensive drilling, demonstrating the value of non-invasive geophysical techniques as a cost-effective alternative for deep groundwater exploration.

2 Methods

This research integrates inadequate drilling information with the geophysical data to estimate *k* for both 2D and 3D evaluations of groundwater resources over the entire investigated site (Fig. 1a). The main stages of the methodology are summarized in the flowchart shown in Fig. 1b.

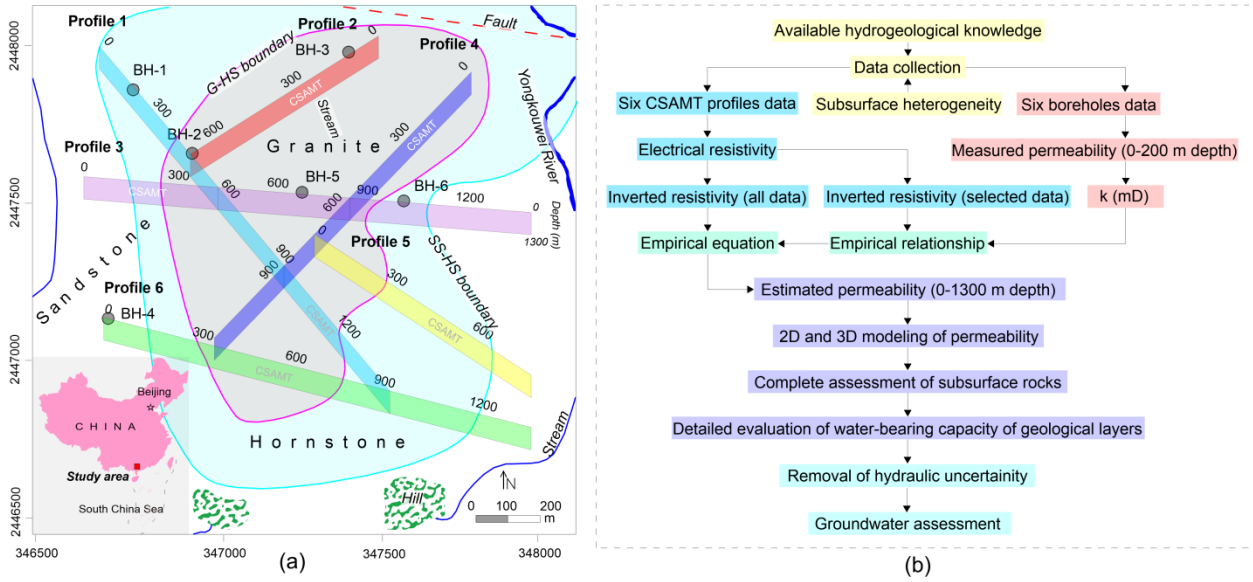

Fig. 1. (a) The site map displaying six boreholes (BH-1 to BH-6) and six CSAMT survey profiles (1–6). The map also illustrates the simplified geological and hydrogeological setting, including the dominant rock types (granite, hornstone, and sandstone), the granite–hornstone (G–HS) and sandstone–hornstone (SS–HS) boundaries, major fault lines, streams, rivers, and surrounding mountainous terrain; (b) Flowchart illustrating the methodology for generating 2D and 3D *k* models to enable comprehensive assessments of groundwater resources across extensive areas

2.1 Study area and hydrogeological settings

This study is part of a national initiative in South Guangdong, China, focused on deep subsurface exploration, including groundwater resource assessment and infrastructure

development such as the Jiangmen Underground Neutrino Observatory (JUNO) (Hasan et al., 2025). These actions contribute to China's national agenda toward sustainable deep-earth resource utilization. This research was conducted in the Jinji region, a geologically complex area prioritized for deep groundwater exploration (Fig. 1a). The region lies within a subtropical monsoonal climate zone, receiving ~1981 mm of annual rainfall. Topography ranges from low hills to mountainous terrain (39–539.9 m elevation), with dense vegetation and varied slopes. The northern part is relatively flat, while the south includes prominent features such as the Dashishan and Qilongding Mountains. Surface drainage is primarily controlled by the Yongkouwei River in the northeast.

Geologically, the Jinji area has evolved through successive tectono-magmatic processes linked to the Yanshanian, Indosinian, and Caledonian mountain-building phases, resulting in a lithologically diverse landscape of granite, sandstone, and hornstone (Qin, 2017). Granite intrusions reflect deep crustal magmatism, while hornstone indicates contact metamorphism. Overlying Paleogene sediments record later basin development. Tectonic structuring in the area is largely influenced by the Kaiping fault-fold complex, which includes reverse, thrust, and strike-slip faults formed under prolonged crustal compression and later modified by strike-slip tectonics. These northeast-trending structures govern subsurface architecture and groundwater flow pathways (Yang et al., 2021). Fractures and joints are widespread in granite, sandstone, and hornstone, varying by lithology and tectonic history. These brittle features act as primary conduits for groundwater, with their alignment along major faults highlighting the tight coupling between structural geology and hydrogeology.

This study focuses on the vertical stratification of aquifer-bearing formations. Productive groundwater is mainly stored in deep, fractured sandstone units, overlain by low-permeability

granite that limits vertical recharge. An intermediate hornstone layer separates the two, with moderate hydraulic properties and limited connectivity. This configuration isolates the deep aquifer from surface influences, rendering shallow investigations ineffective. Deep-targeted exploration is thus essential for identifying and managing these concealed high-potential groundwater resources in a structurally complex hard rock setting.

2.2 CSAMT survey

2.2.1 Theoretical background

CSAMT is extensively employed for hard rock evaluations due to its ability to resolve deep subsurface features (Fu et al., 2013; Wang et al., 2015; Di et al., 2020; Kouadio et al., 2023). This method employs a distant, regulated electric source that transmits signals into the ground, while electric and magnetic field components are recorded at receiving stations (Zonge and Hughes, 1991). CSAMT uses frequency-dependent EM wave penetration; lower frequencies reach greater depths, depending on rock conductivity (Cagniard, 1953; Borah and Patro, 2019). Signal frequencies are extracted using Fourier transforms from time-series field measurements (Simpson and Bahr, 2005). A typical CSAMT setup uses electric dipole sources arranged between 1 and 2 km intervals, with 5–10 km offsets based on the required penetration depth and lithological conditions.

Resistivity is calculated by analyzing orthogonal electric and magnetic field magnitudes. Vertical resolution typically ranges from 5%–20% of the depth of investigation (DOI), which spans ~20–1000 m. Shallow depths (20–100 m) offer finer resolution, while deeper imaging is coarser due to signal attenuation. DOI increases with lower frequencies and higher subsurface resistivity (Borah and Patro, 2019). Lateral resolution depends on station spacing (10–200 m);

wider spacing enhances signal strength and coherence (Simpson and Bahr, 2005). Field setups include portable receivers with electrodes and magnetic sensors to record signals, which are filtered and amplified in real time. Effective survey planning is essential to mitigate interference from fences, power lines, and radio transmitters. Final resistivity models are presented in plan, fence, cross-sectional, or 3D formats.

2.2.2 Survey design and procedures

Data acquisition was performed along six CSAMT lines (1–6) using a 50 m interval between stations, selected based on geological targets, terrain accessibility, structural orientation, integration with borehole data, and expected resistivity contrasts. These optimized profiles improved subsurface resolution and minimized interpretational ambiguity. The DOI reached approximately 1300 m. Measurements were conducted in scalar Transverse Magnetic (TM) mode, recording E- and H-field vectors in both longitudinal and transverse directions along the survey profiles. EMAP stations were spaced ~50 m from electrodes. A 50 Hz linear filter was implemented under Gain Mode X1 settings. Transmission current spanned 2.6–18 A across the 7680 Hz to 1 Hz range.

Data acquisition utilized a Phoenix Geophysics V8 multifunction receiver and TXU-30 transmitter, capable of 30 kW output, transmitting up to 1000 V and 40 A. The system operated across 34 frequencies (1–7680 Hz), with transmitter–receiver distances of 9.3–12.5 km. Non-polarized electrodes captured electric fields, while magnetic fields were recorded using AMTC-30 sensors (0.1–10,000 Hz). Each site recorded two orthogonal electric and three orthogonal magnetic components, enabling full impedance tensor calculation. Survey positions were determined using Hi-Target V30 RTK and Trimble XH GPS, ensuring sub-meter accuracy. Coordinates were computed and transmitted to the navigation system for real-time positioning.

Survey point spacing remained consistent, with system quality metrics indicating 3–5% variability. Design tolerances were met: RMS error < ±5%, inter-point error < 10%, horizontal and vertical tolerances of 2.33 mm and 1.67 mm, respectively. Minimal anthropogenic and electrical interference at the site resulted in high-quality data. Final site interpretation was based on rigorous CSAMT data processing, including skew filtering and curve analysis (Hasan et al., 2025).

2.2.3 Processing workflow

Spatial filters (Hanning window) and static corrections were applied to refine resistivity data and enhance the model accuracy. The static corrections addressed near-surface resistivity inhomogeneities that cause vertical shifts in apparent resistivity curves. By calibrating electric field measurements to a stable reference, shallow-layer effects were minimized, isolating deeper signals. Spatial filtering using a Hanning window reduced high-frequency noise while preserving coherent spatial patterns. This approach significantly improved inversion model stability by suppressing spectral leakage and smoothing fluctuations. Data processing was carried out using the CMTPro version software produced by Phoenix Geophysics (Phoenix Geophysics CMTPro, 2020), which integrates V8 and tracking data, corrects coordinates, smoothes curves, and exports files for inversion. Based on CSAMT-SW technique, the processing workflow shown in Fig. 2 (Phoenix Geophysics CSAMT-SW, 2020) was conducted to obtain 2D inversion (Rodi and Mackie, 2001; Wang et al., 2015).

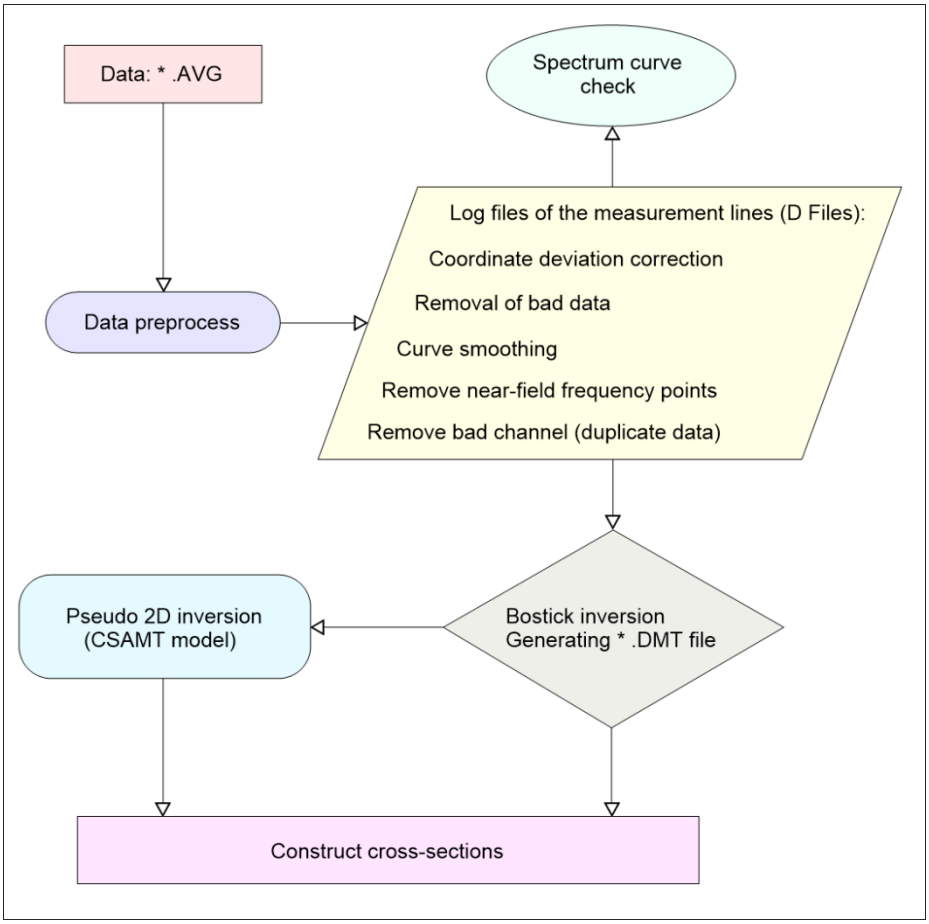

Fig. 2. Schematic of the 2D CSAMT data inversion workflow using Bostick methodology

The main components of the CSAMT-SW framework are: 1. Transformation from AVG to D format; 2. Editing CHK data and converting to D format; 3. Manual data checks: gap filling, near-field removal; 4. Smoothing based on D-format data; 5. Estimation of correction factors (D, H, K, Z); 6. The Bostick inversions; 7. The Quasi-2D inversions using the global field model (ID), integrating near and transition fields. Post-Bostick inversion results were stored as *_BOS.DAT and *_BSS.DAT, with final inversion-ready data in *_M.DMT. The 2D inversion proceeded until either the RMS error threshold or a five-iteration limit was reached. Final resistivity models (Fig. 3) were cross-validated with local geology and clearly delineated subsurface features, offering a robust interpretation framework.

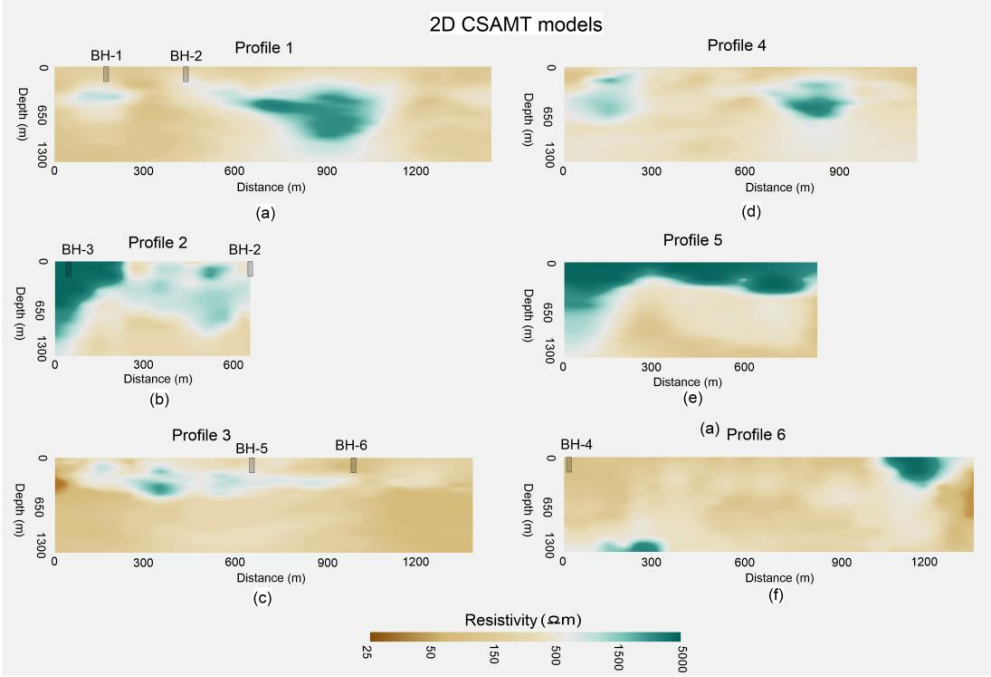

295

296 **Fig. 3.** Construction of 2D CSAMT models along six geophysical surveyed lines: (a) Line 1, (b) Line 2,
297 (c) Line 3, (d) Line 4, (e) Line 5, and (f) Line 6. Resistivity values increase from brown to green on the
298 color scale.

299 ## 2.3 Permeability estimation framework

300 ### 2.3.1 Laboratory-based permeability determination from borehole core samples

301 Permeability is a key hydrogeological parameter that quantifies the ability of porous media, such
302 as rock or sediment, to transmit fluids. It governs subsurface fluid flow and plays a central role in
303 groundwater studies (Allègre et al., 2016; Fiandaca et al., 2018; Mudunuru et al., 2022;
304 Esmaeilpour et al., 2023; Carbillet et al., 2024). Permeability reflects how easily fluids move
305 through pore networks or fractures and is typically measured via pumping tests or core analysis,
306 methods that are costly and logistically intensive. It is influenced by porosity, lithology,
307 saturation, structural features (e.g., faults, joints), and diagenetic processes (Dewandel et al.,
308 2006; Yan et al., 2024).

In the present work, initial k data from the Jinji region were limited to six boreholes. To strengthen the dataset, 116 lab tests were conducted on core samples from three main lithologies, sandstone (31), hornstone (23), and granite (62), recovered from depths up to 200 m. These data help delineate vertical k trends and refine the region's hydrogeological model. Core recovery employed a wireline rotary system with triple-tube barrels to preserve sample integrity (ISRM, 2015). Samples were vacuum-sealed and stored under controlled humidity to retain in-situ moisture and fracture structure. Prior to testing, cores were trimmed to standard 50 mm × 100 mm cylinders and screened for visible defects. Two laboratory methods were used based on k range. The steady-state flow test with ASTM D5084-21 guidelines (ASTM, 2021) was applied to higher-k sandstone. A constant hydraulic gradient was applied under fully saturated conditions, and the corresponding volumetric flow rate was recorded. Permeability was determined through the application of Darcy's Law:

$$k = \frac{Q \cdot \mu \cdot L}{A \cdot \Delta P} \quad (1)$$

where ΔP shows the pressure differential applied across the sample (Pa), A represents the cross-sectional area (m^2), L indicates the length of the sample (m), μ shows the dynamic viscosity of the fluid (Pa·s), and Q denotes the volumetric flow rate (m^3/s).

For low-k hornstone and granite, the pulse decay method (Brace et al., 1968) was used. A brief pressure pulse was applied, and pressure decay was monitored under confining stresses up to 30 MPa to simulate in-situ conditions and assess stress-dependent k behavior. Tests were conducted under both dry and saturated conditions to evaluate moisture sensitivity. Replicate measurements ensured data reliability, and statistical analyses assessed intra- and inter-lithology variability. Results revealed that granite had the lowest k due to its dense crystalline structure,

while hornstone showed intermediate values, likely due to localized fracturing. Sandstone exhibited the highest *k*, particularly at greater depths, confirming its role as the primary aquifer unit in the region.

2.3.2 Permeability-resistivity relationship: Archie's law and the role of Kozeny–Carman

Numerous foundational studies have linked electrical resistivity to hydraulic properties like *k*. A prominent example is the Archie equation (Archie, 1942), which relates resistivity to porosity and water saturation in clean, saturated sediments. However, its assumption of clay-free conditions limits its applicability in complex or clay-rich lithologies. (Waxman and Smits, 1968; Glover, 2015). It is commonly expressed as:

$$\rho b = a \cdot \rho f \cdot \phi^{-m} \qquad (2)$$

In this equation, ϕ represents porosity, ρf indicates fluid resistivity, ρb denotes bulk resistivity, and a and m are empirical constants. Although Archie's law does not directly yield *k*, porosity serves as a useful proxy due to its strong influence on fluid movement. As such, the resistivity–porosity relationship can be leveraged to infer *k* indirectly, especially when supplemented with additional petrophysical frameworks (Revil & Cathles, 1999).

The Kozeny–Carman equation, though not used explicitly in this study, provides a widely accepted theoretical foundation that connects *k* to porosity and specific surface area (Carman, 1956; Bear, 1972). While it does not incorporate resistivity directly, this model is often used in hydrogeophysical studies to support the interpretation of petrophysical relationships that bridge electrical and hydraulic properties (Chapuis and Aubertin, 2003). Its relevance lies in the broader theoretical justification for using porosity, derived or inferred from resistivity, as a predictor of *k*.

The application of this equation alongside Archie's law facilitates the development of empirical or semi-empirical models that connect electrical resistivity to *k* (Glover, 2009; Yan et al., 2024).

However, direct application of these equations to complex geological environments, such as fractured granite, sandstone, and hornstone, remains limited due to heterogeneities in mineral composition, pore connectivity, and structural anisotropy. To mitigate such constraints, our approach empirically develops a localized, site-calibrated correlation involving *k* and resistivity, grounded in co-located deep borehole and CSAMT data. This empirical link supports high-resolution spatial modeling of *k* in both 2D and 3D for the Jinji area, offering enhanced insight into subsurface hydrogeological conditions where traditional models may not be applicable.

2.3.3 Spatial permeability modeling from CSAMT data

To estimate permeability across the entire study area, we implemented a multi-stage approach integrating borehole core analysis with CSAMT-derived resistivity data. In the first stage, a total of 116 laboratory-based *k* measurements were acquired using 6 drilling tests (from BH-1 to BH-6) with 0–200 m depth (Fig. 4). The *k* measurements were obtained from intact rock core samples representing three principal lithologies: granite, hornstone, and sandstone.

In the second stage, each of the 116 borehole-derived *k* values was empirically correlated with corresponding resistivity values extracted from CSAMT soundings co-located with the borehole sites. The spatial correspondence between boreholes and CSAMT sounding points was carefully matched (Fig. 4). For example: P1-5 represents the fifth CSAMT sounding at 200 m along survey line 1 near borehole BH-1; P1-9 corresponds to the ninth sounding at 400 m on line 1 near borehole BH-2; P2-3 denotes the third sounding at 100 m along line 2 near BH-3; P6-1 indicates the first sounding at 0 m on line 6 adjacent to BH-4; P3-15 and P3-21 represent the

fifteenth (700 m) and twenty-first (1000 m) soundings along line 3, near boreholes BH-5 and BH-6, respectively.

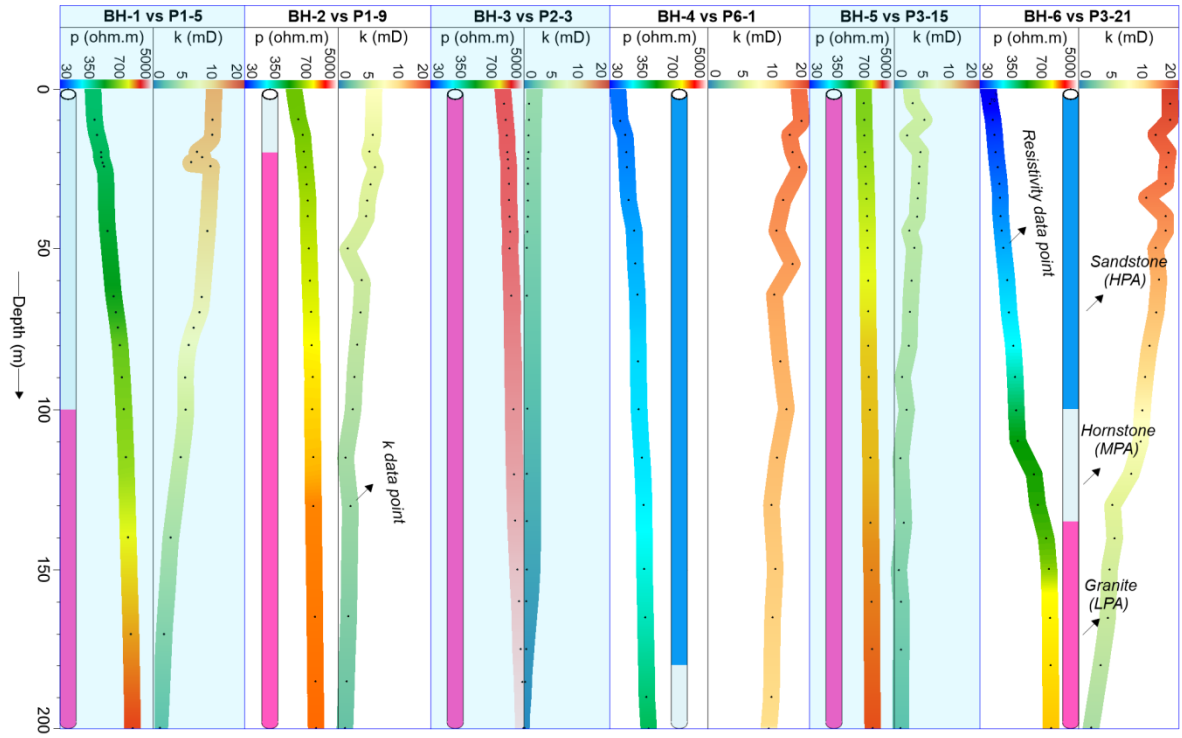

Fig. 4. Comparison of 116 CSAMT-based resistivity (ρ) data points with corresponding drilling-based permeability (k) values at depths of 0–200 m across six borehole locations (BH-1 to BH-6). The data were used to evaluate high potential aquifers (HPA) in sandstone, medium potential aquifers (MPA) in hornstone, and low potential aquifers (LPA) in granite. Each dot represents a resistivity or permeability data point. Sounding labels indicate specific CSAMT locations: P1-5 (5th point on line 1), P1-9 (9th on line 1), P2-3 (3rd on line 2), P6-1 (1st on line 6), and P3-15 and P3-21 (15th and 21st on line 3.)

In the third stage, all 116 paired measurements of permeability (k) and resistivity (ρ) were utilized to develop an empirical model. An exponential relationship was derived between permeability (k in millidarcies or mD) and electrical resistivity (ρ in Ωm), expressed as follows (Fig. 5):

$$k = 15.373(e)^{-0.002(\rho)} \quad (3)$$

This site-specific empirical model was then applied to the entire suite of CSAMT resistivity data collected along six survey profiles to estimate spatial variations in *k* across the broader study area. Using this relationship, we generated predictive 2D and 3D *k* models that capture the hydraulic behavior of three major lithological units: low potential aquifer (LPA): associated with low-permeability granite, medium potential aquifer (MPA): hosted within fractured hornstone (hornfels), high potential aquifer (HPA): corresponding to more porous sandstone units.

These models provide a depth-resolved assessment of subsurface *k* reaching depths of up to 1300 m below the surface. Final 2D and 3D spatial visualizations were developed by SKUA-GOCAD and Geosoft Oasis montaj modeling software (Webring, 1981; Mira Geoscience Ltd., 1999; Hasan et al., 2024), enabling the visualization of *k* distributions across all six CSAMT profiles and improving hydrogeological characterization in structurally complex hard rock terrain.

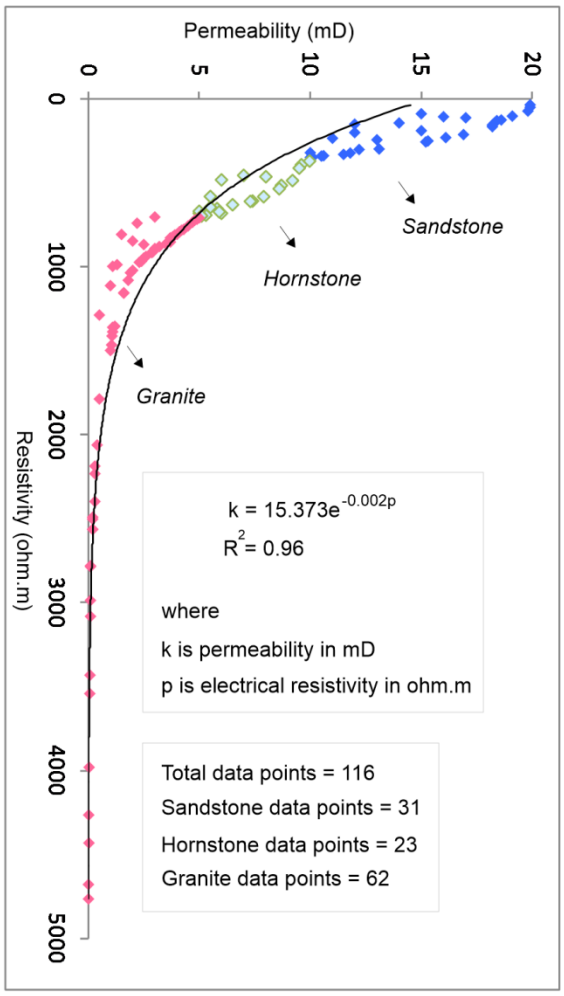

Fig. 5. Empirical relationship derived from 116 data points comparing CSAMT-based resistivity and drilling-based *k* at depths of 0–200 m, across three lithologies: sandstone (31 data points), hornstone (23 data points), and granite (62 data points).

3 Results

3.1 Cross-validation of geophysical and borehole parameters

Table 1 summarizes the integrated dataset from 6 drills and 6 geophysical profiles to resolve the spatial structure of the subsurface into three distinctive hydrogeological units, based on variations in electrical resistivity and corresponding *k* values. The development of these

subsurface models mainly depends on borehole data, CSAMT-derived resistivity measurements, and the regional geological framework. The stratigraphy was categorized into three primary lithologies: sandstone, hornstone, and granite. Classification criteria were established as follows: sandstone was defined by resistivity values below 350 Ωm and a *k* range of 10–20 mD; hornstone exhibited resistivity values between 350 and 700 Ωm with a k range of 5–10 mD; and granite was characterized by resistivity values exceeding 700 Ωm and *k* values ranging from 0 to 5 mD. Based on our evaluations of the subsurface hydrogeological model's aquifer potential zones, we found that sandstone contains the high potential aquifer (HPA), hornstone contains medium potential aquifer (MPA), and granite has low potential aquifer (LPA). Aquifers with the largest yields or the best water-bearing capacity are indicated by sandstone, whereas aquifers with the lowest yields or the worst water-bearing capacities are denoted by granite. Groundwater development is best facilitated by sandstone in the study area, whereas groundwater extraction is most hindered by granite.

Table 1

Integrating distinct ranges of electrical resistivity and *k* enables a comprehensive assessment of groundwater potential across various hard rock types

Resistivity (Ωm)	*k* (mD)	Type of rock	Aquifer potential
< 350	10–20	Sandstone	High potential aquifer (HPA)
350–700	5–10	Hornstone	Medium potential aquifer (MPA)
>700	0–5	Granite	Low potential aquifer (LPA)

3.2 2D groundwater assessments

425 Using geophysical-borehole correlation as its basis, Eq. (3) efficiently converts 2D CSAMT
426 models (Fig. 3) into 2D *k* models (Fig. 6). The interpreted 2D *k* models shown in Fig. 7, in
427 comparison with the limited borehole experiments, allow for a comprehensive assessment of the
428 groundwater resources in hard rock across the whole research area, from 0 to 1300 m deep.

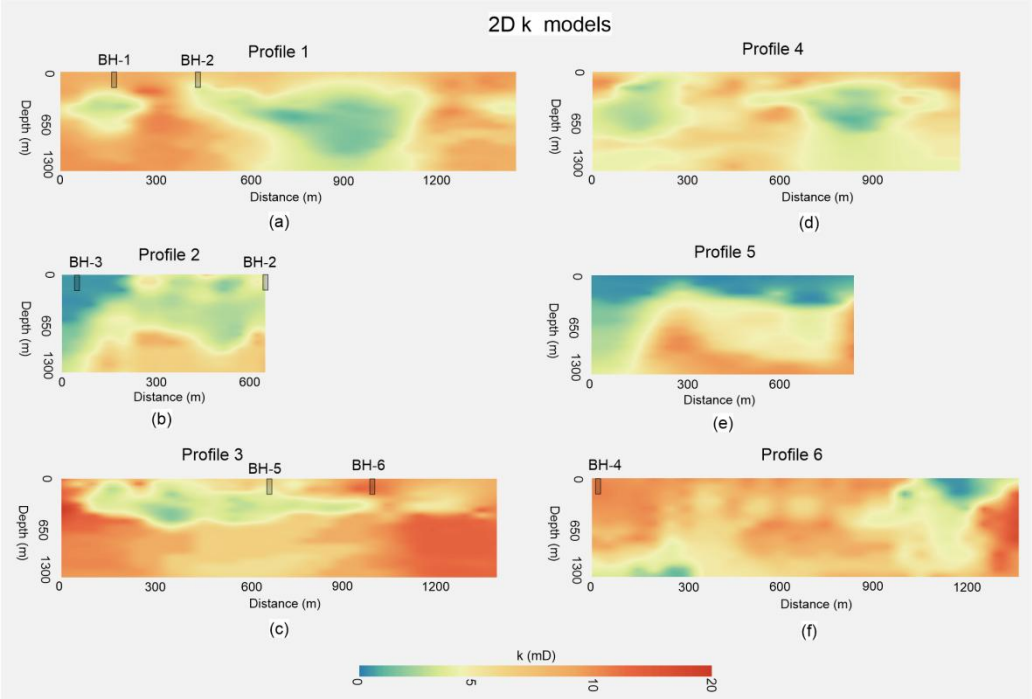

429

430 **Fig. 6.** The predicted 2D *k* models along six geophysical surveyed lines: (a) Line 1, (b) Line 2, (c) Line 3,
431 (d) Line 4, (e) Line 5, and (f) Line 6. *k* values increase from blue to red on the color scale.

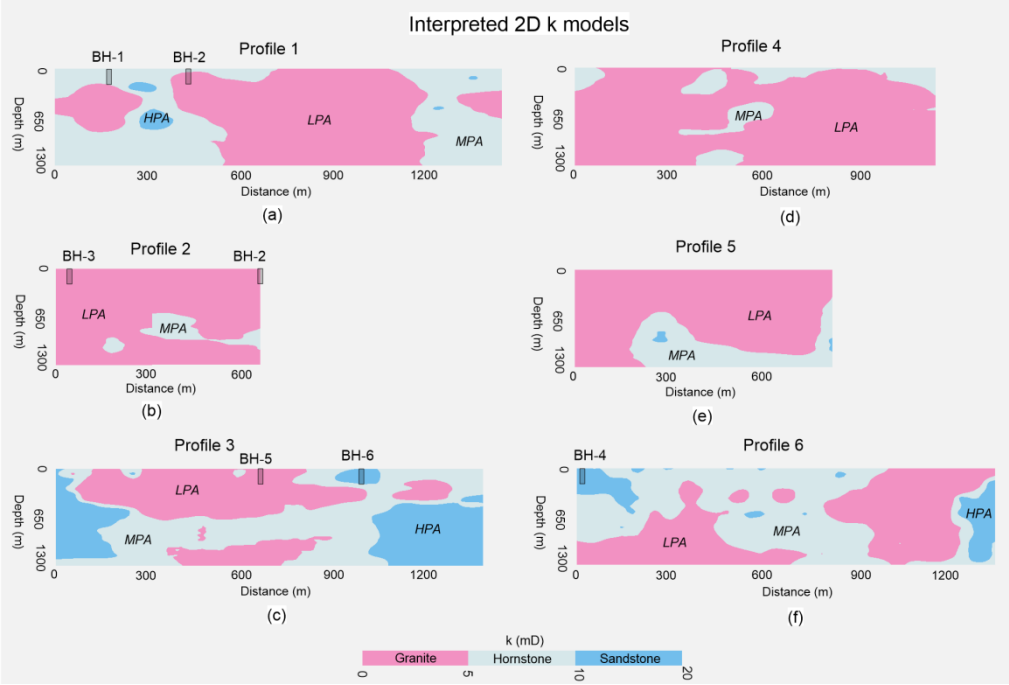

Fig. 7. The interpretation of the predicted 2D *k* models along six geophysical surveyed lines: (a) Line 1, (b) Line 2, (c) Line 3, (d) Line 4, (e) Line 5, and (f) Line 6. Sandstone is represented in blue, hornstone in light blue, and granite in pink

The integrated 2D *k* models (Fig. 8) and their interpretations (Fig. 9) provide a detailed evaluation of groundwater potential across complex geological settings of sandstone, hornstone, and granite. Profile 1 reveals a high-potential sandstone aquifer (85–305 m thick) between 245–380 m distances at 205–400 m depth. Medium-potential hornstone aquifers are found from 0–525 m and 1185–1445 m distance down to 1300 m. Low-potential granite aquifers appear at 0–285 m (290–790 m depth), 385–1185 m (full depth), and 1305–1450 m (390–745 m depth). Profile 2 shows a medium-potential hornstone aquifer with 140–380 m thickness (490–1105 m depth) between 145–215 m and 290–645 m distance. No high-potential sandstone aquifers are present. Granite dominates (0–700 m distance, 0–1300 m depth) the profile with low yield except in hornstone zones. Profile 3 contains both high-potential sandstone (0–250 m, 905–1065 m, and

1040–1390 m distances at respective depths of 0–1190, 0–205, and 490–1305 m) and medium-potential hornstone aquifers (full depth with 0–1400 m distance) across the entire surveyed line. Granite aquifers are assessed at 80–1015 m (0–590 m depth), 395–845 m (915–1300 m depth), and 1100–1300 m (200–500 m depth). Profile 4 features medium-potential hornstone at 0–105 m (0–340 m depth), 340–645 m (0 to 1300 m depth), 595–790 m (0–300 m depth), and 1015–1145 m (0–345 m depth). No high-potential sandstone is observed. Granite aquifers of low potential dominate (0–1145 m distance between 0–1300 m depth), except in hornstone zones. Profile 5 shows medium-potential hornstone (190–845 m distance, 390–1300 m depth) and two small high-yield sandstone patches (290 m at 790–960 m depth and 815 m at 1045–1135 m depth). Low-potential granite appears at distance 0–190 m (0–1300 m depth) and 790–815 m (0–1025 m depth). Profile 6 includes high-potential sandstone zones at 0–190 m (0–490 m depth) and 1245–1345 m (215–1225 m depth). Low-potential granite is present at 0–690 m (390–1300 m depth) and 790–1360 m (0–1190 m depth), while hornstone with medium potential dominates the remainder. Overall, the southeastern and northwestern zones host abundant medium- to high-potential aquifers, while central regions show limited or poor groundwater prospects.

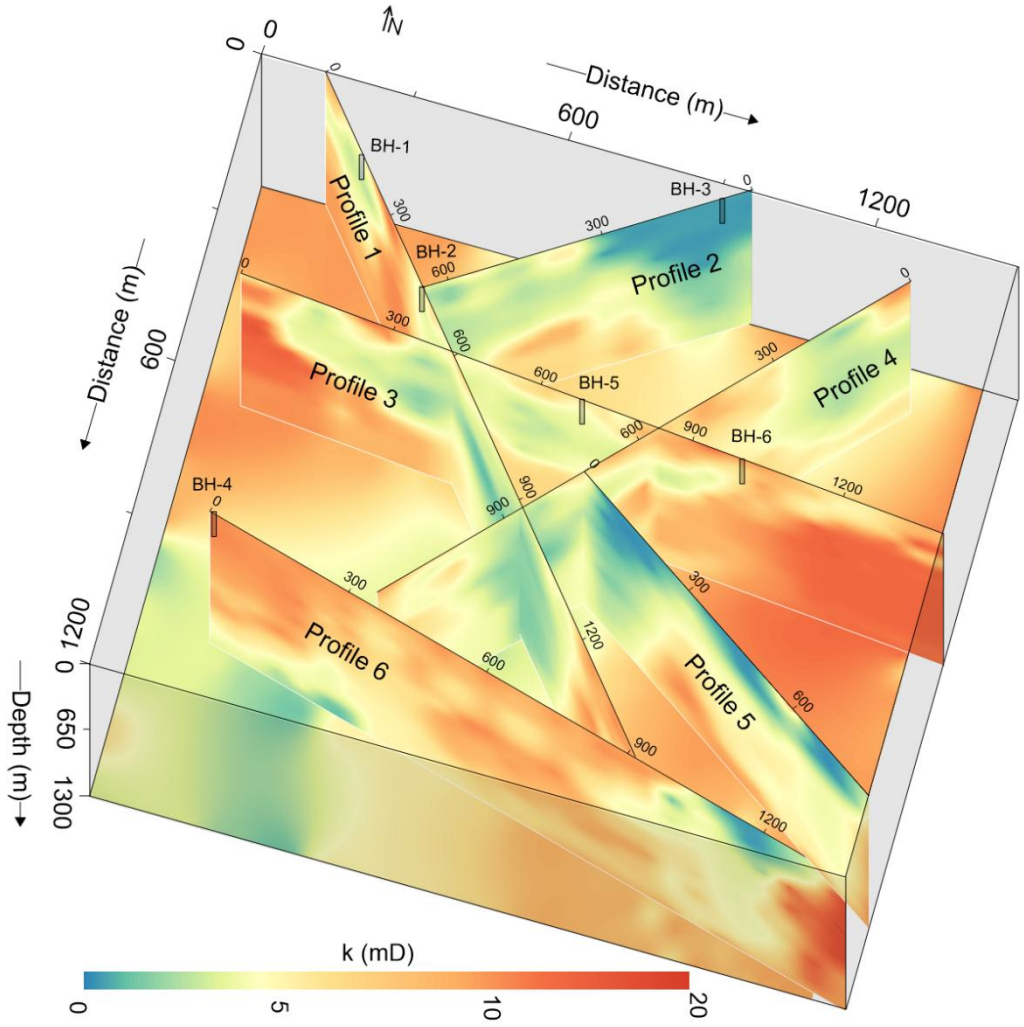

461

462 **Fig. 8.** The integrated 2D *k* models derived from the incorporation of geophysical and drilling data, with *k*

463 represented on a color bar spanning from green to red

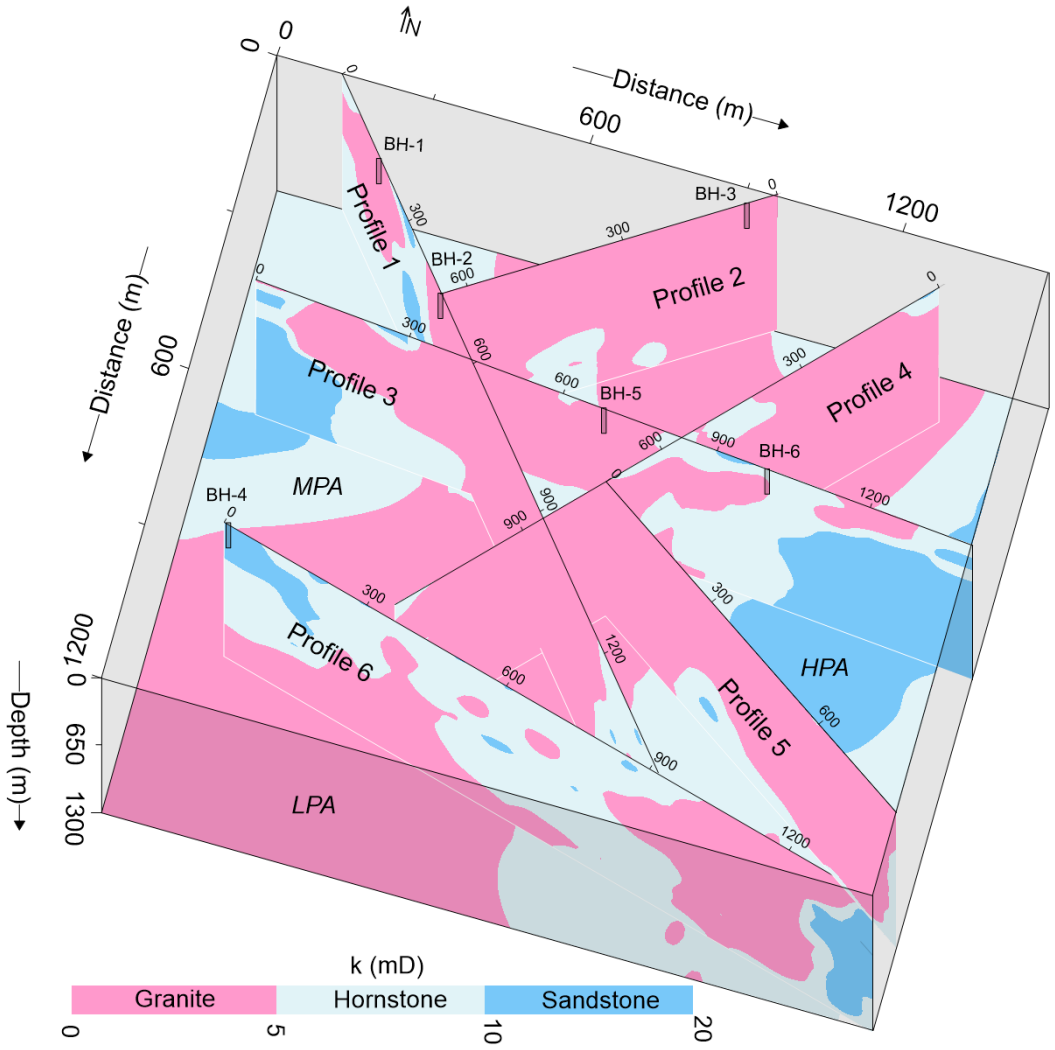

464

465 **Fig. 9** Analysis of 2D *k* models, based on defined *k* ranges, for three groundwater potential aquifers: low
466 potential aquifer (LPA), medium potential aquifer (MPA), and high potential aquifer (HPA),
467 corresponding to the granite, hornstone, and sandstone formations, respectively

468 **3.3 3D groundwater assessments**

469 The 3D *k* (outer view) visualization (Fig. 10a, b) provides a comprehensive assessment of the
470 water-bearing capacity of the rock mass. Low-potential granite aquifers are found at the surface
471 along: line 1 (85–215 m, 385–1175 m), line 2 (0–655 m), line 3 (0–45 m, 95–175 m, 265–585 m,
472 605–845 m, 1145–1315 m), line 4 (90–390 m, 490–615 m, 745–1115 m), line 5 (0–815 m), and

line 6 (1045–1345 m). Medium-potential hornstone aquifers appear along: line 1 (0–95 m, 190–260 m, 295–415 m, 1185–1425 m), line 3 (40–105 m, 215–275 m, 580–605 m, 850–910 m, 1010–1155 m, 1310–1410 m), line 4 (45–90 m, 390–490 m, 590–685 m, 1115–1185 m), and line 6 (90–190 m, 215–275 m, 315–485 m, 505–605 m, 635–1045 m). High-potential sandstone aquifers are identified in: line 1 (265–310 m), line 3 (235–255 m, 915–1010 m), line 4 (0–45 m), and line 6 (0–90 m, 210–225 m, 275–305 m, 515–525 m, 605–635 m), Overall, Fig. 10 (a, b) shows that higher-yield aquifers are mainly concentrated in the southern portion of the investigated site.

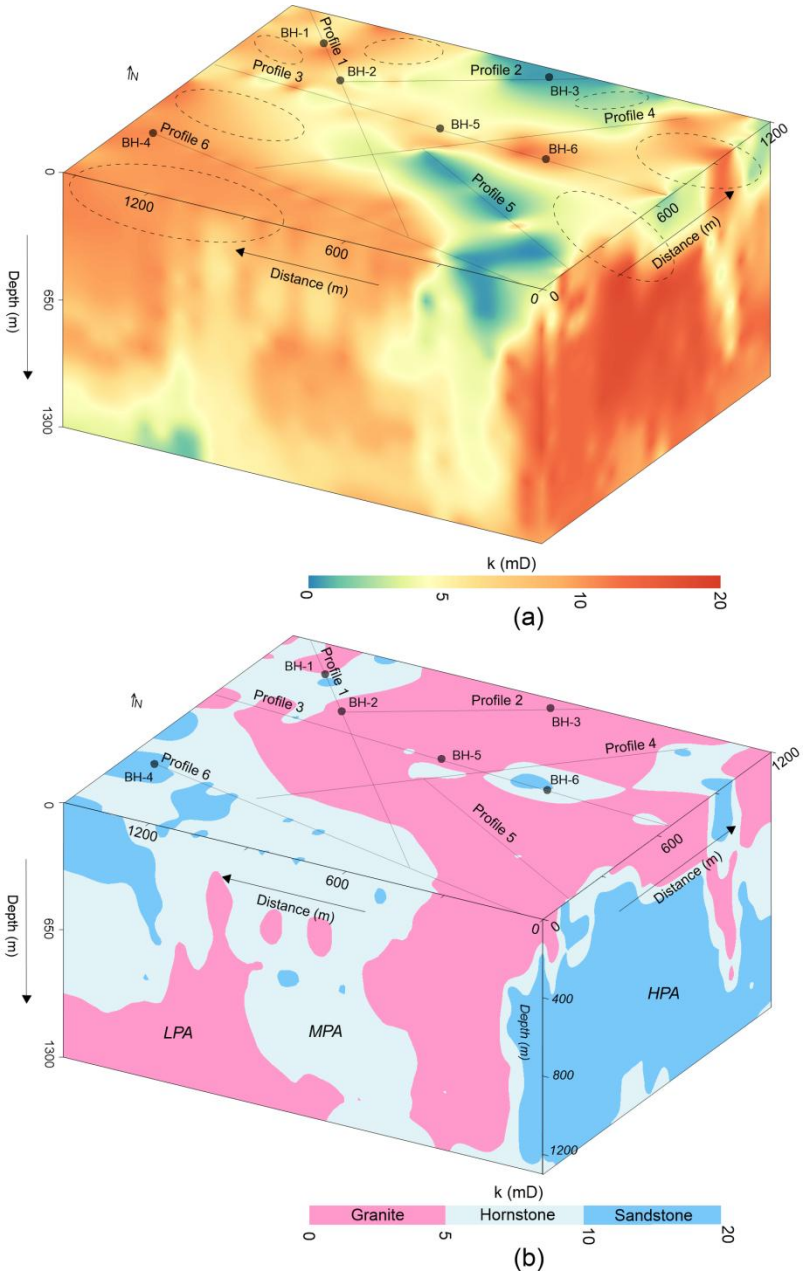

Fig. 10. The 3D *k* models (CSAMT-based), with *k* shown on a color scale increasing from green to red, correspond to three groundwater potential aquifers: low potential aquifer (LPA), medium potential aquifer (MPA), and high potential aquifer (HPA), associated with three geological strata: granite, hornstone, and sandstone, respectively. The uncertainty contours (highlighted by areas with black dots) indicate zones of reduced confidence in *k* estimation. (a) The exterior visualization of the 3D *k* model, and (b) The analysis of the 3D *k* model from an external perspective

Fig. 11 (a, b) shows a 3D internal view of aquifer potential at 1300 m depth. Low-yield granite aquifers are identified along: surveyed line 1 (515–1215 m), line 2 (0–290 m), line 3 (390–690 m), line 4 (0–1145 m), line 5 (0–195 m, 565–595 m), and line 6 (0–690 m, 1075–1115 m). Medium-potential hornstone aquifers are found along: profile 1 (0–540 m, 1215–1445 m), profile 2 (295–675 m), profile 3 (175–395 m, 445–815 m, 915–1035 m), profile 5 (205–565 m, 610–815 m), profile 6 (685–1080 m, 1110–1355 m). High-potential sandstone aquifers appear along: profile 3 (0–205 m, 1010–1400 m) and profile 5 (810–815 m). Overall, medium to high potential aquifers are mainly distributed in the southeastern and northwestern regions, while central areas are dominated by low-yield granite. The aerial 3D *k* model enhances visualization of aquifer distribution, supporting accurate groundwater assessment.

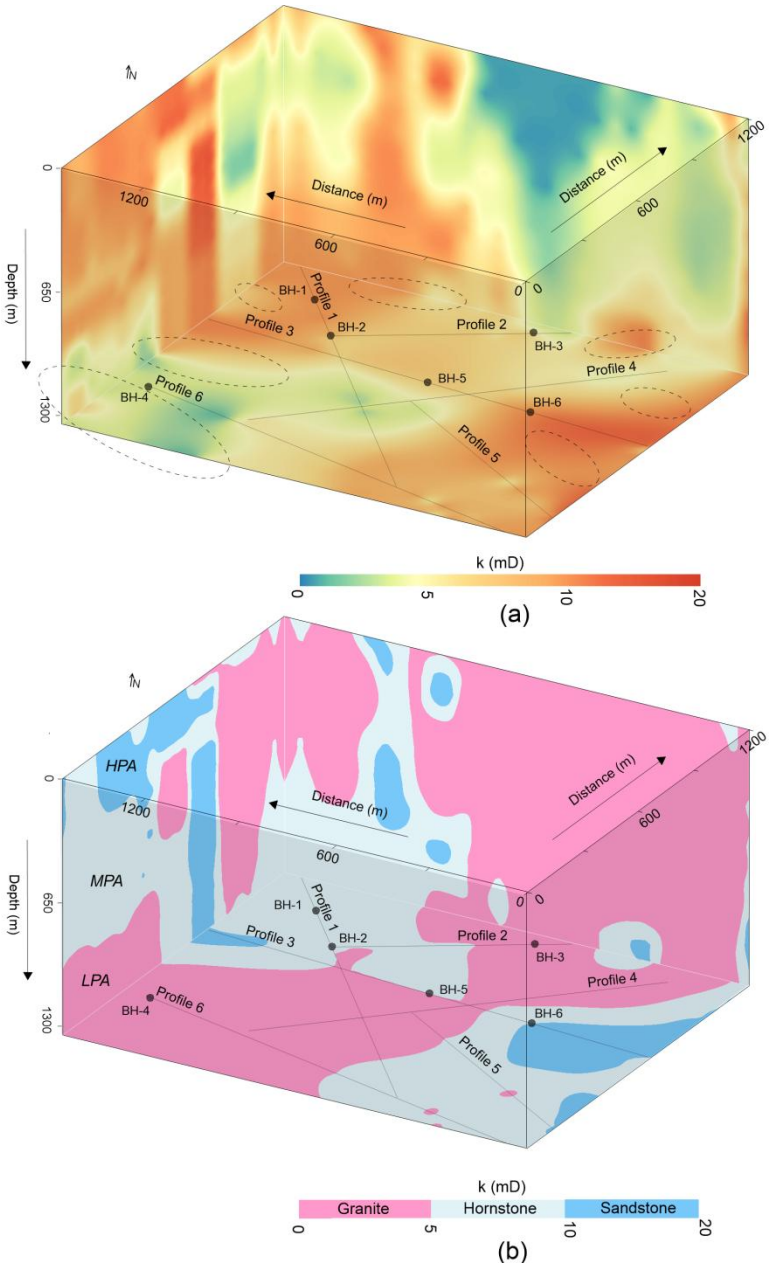

498

499 **Fig. 11.** The 3D *k* models (CSAMT-based), with *k* represented on a color scale ranging from green to red,
500 illustrate three groundwater potential aquifers: low potential aquifer (LPA), medium potential aquifer
501 (MPA), and high potential aquifer (HPA), associated with three geological strata: granite, hornstone, and
502 sandstone, respectively. The uncertainty contours (highlighted by areas with black dots) indicate zones of
503 reduced confidence in *k* estimation. (a) The interior visualization of the 3D *k* model, and (b) The analysis
504 of the 3D (internal perspective) *k* model

3.4 Depth-wise groundwater assessments

Due to limited borehole data, direct estimation of *k* below 200 m is not feasible. However, by integrating borehole and CSAMT data, *k* values could be reliably estimated down to 1300 m. This approach enabled efficient and detailed evaluation of hard rock aquifers using both 2D and 3D models (Fig. 12), with *k* values extracted at depths of 0, 200, 600, 1000, and 1300 m. At 1300 m, over 42% of the subsurface in the southwest and northeast comprised low-yield granite. Hornstone accounted for 40% (medium yield) near granite zones in the northwest and southeast, while high-yield sandstone made up 18% in the east. At 1000 m, sandstone (15%) was concentrated in the southeast (high yield), hornstone (38%) in the southeast and northwest (medium yield), and granite (47%) dominated the central and boundary zones (low yield). At 600 m, the subsurface was 55% granite (central and northern zones, low yield), 32% hornstone (western region, medium yield), and 13% sandstone (southeast, high yield). At 200 m, granite dominated 64% of the center and north (low yield), hornstone made up 26% in the south (medium yield), and sandstone (10%) in the west was associated with high yield. At 0 m, 73% of the central area comprised low-yield granite, 20% of the southwest was hornstone (medium yield), and 7% sandstone (high yield) was concentrated in the southwest.

Overall, Fig. 12 shows a decrease in low-yield granite thickness with depth. Groundwater potential is lowest around 600–700 m depth, while deeper zones (>700 m) in the northwest, southeast, and southwest show more favorable aquifer conditions.

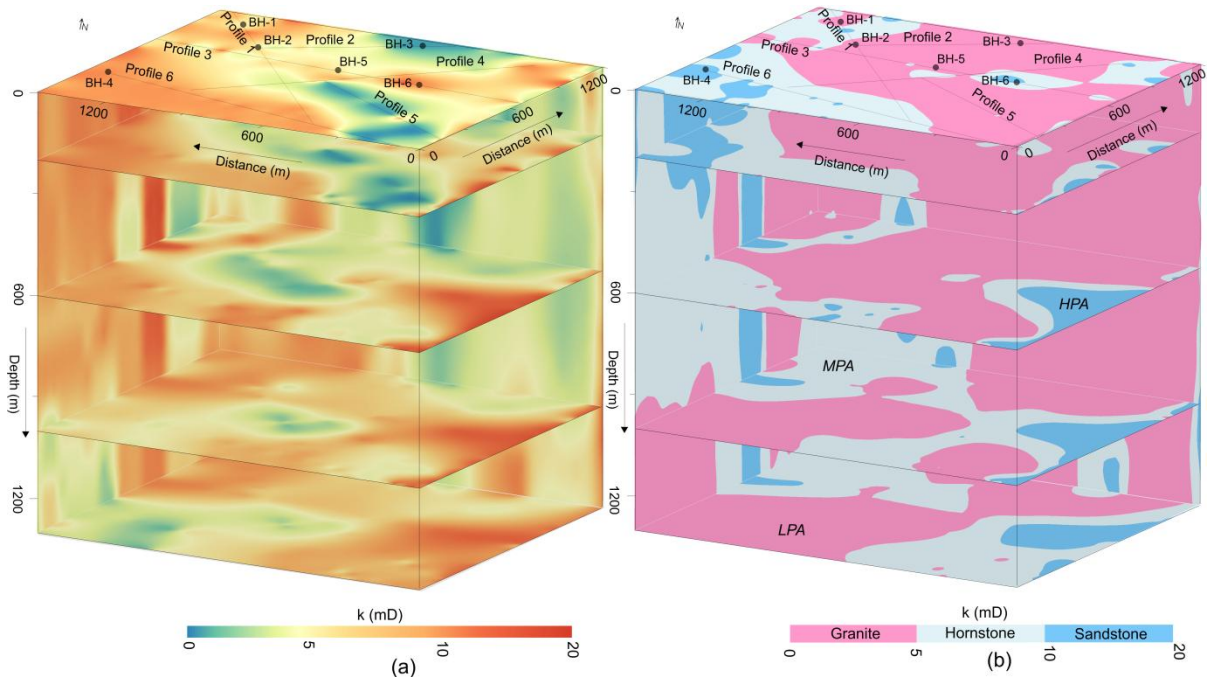

Fig. 12. (a) Geophysical *k* imaging at depths of 0, 200, 600, 1000, and 1300 m, with *k* shown on a color scale increasing from green to red. (b) Evaluation of CSAMT-derived *k* values (based on defined *k* ranges) at various depths for different aquifer types: low potential aquifer (LPA) in granite, medium potential aquifer (MPA) in hornstone, and high potential aquifer (HPA) in sandstone

3.5 Validation of predicted vs. measured permeability

Groundwater evaluation was greatly improved by systematic CSAMT-based *k* estimation. As shown in Figs. 6–12, granite dominates the central, northeastern, and southwestern zones; hornstone occurs mainly in the southeast, west, and northwest; and sandstone is prevalent in the east. Borehole-based assessments are limited by inconsistent subsurface mapping. While *k* values align near 200 m depth, broader extrapolation remains uncertain, highlighting the limitations of sparse drilling in complex geology.

To clarify the basis of the percentage matching values, the following explicit equation was used to quantify the agreement between CSAMT-derived *k* values and borehole-based *k* estimates:

$$\text{Percentage Matching} = \left(\frac{Ns}{Nl}\right) \times 100 \qquad (4)$$

Here, N_s represents the smaller of the two *k* values, either from the CSAMT model or borehole data, at a given depth, while N_l is the larger. This ratio offers a normalized agreement metric, where 100% indicates a perfect match and lower values reflect greater divergence. Comparisons were made at multiple depth intervals across six calibration boreholes. Table 2 summarizes the percentage agreement for 18 selected data points (out of 116) between measured and predicted *k* values. Agreement was calculated at matched depth intervals for each borehole–sounding pair using Eq. (3). For example, BH-1 and P1-5 show 73%, 63%, and 100% agreement at 10, 40, and 170 m depth. BH-2 and P1-9 exhibit 80%, 77%, and 85% agreement at 20, 60, and 185 m depth. Other pairings, such as BH-3 with P2-3, show lower agreement (67%, 40%, 30%) at 10, 85 and 200 m depth, while BH-5 and P3-15 yield high matches of 80%, 94%, and 85% at 30, 135, and 200 m depth, and BH-6 and P3-21 produce matches of 61%, 74%, and 71% at 45, 165, and 180 m depths, respectively.

Overall, the results indicate strong consistency between observed and predicted values, with discrepancies likely due to local heterogeneity or measurement uncertainty. Even at lower percent match, both methods often classify the site into the same aquifer potential zone, supporting the robustness of the CSAMT-based approach for regional groundwater assessment.

Table 2

557 Percentage match and deviation between the measured *k* and the predicted *k* for 18 selected data points
558 out of the total 116

CSAMT data points (selected)			Drilling data			%Matching	Difference
CSAMT sounding number	Resistivity (Ωm)	Predicted *k*' (mD) using Eq. (3)	Borehole name	Depth (m)	Measured *k* (mD)	*k'* vs *k*	between *k'* and *k*
P1-5	392	7.0	BH-1	10	9.6	73	2.6
P1-5	515	5.5	BH-1	40	8.7	63	3.2
P1-5	1080	1.8	BH-1	170	1.8	100	0.0
P1-9	669	4.0	BH-2	20	5.0	80	1.0
P1-9	863	2.7	BH-2	60	3.5	77	0.8
P1-9	1354	1.02	BH-2	185	1.2	85	0.18
P2-3	2187	0.2	BH-3	10	0.3	67	0.1
P2-3	2988	0.04	BH-3	85	0.1	40	0.06
P2-3	4765	0.003	BH-3	200	0.01	30	0.007
P6-1	50	13.9	BH-4	15	19.9	70	6.0
P6-1	200	10.3	BH-4	100	12.0	86	1.7
P6-1	348	7.7	BH-4	180	9.9	78	2.2
P3-15	792	3.3	BH-5	30	4.1	80	0.8
P3-15	1157	1.5	BH-5	135	1.6	94	0.1
P3-15	1412	0.91	BH-5	200	1.07	85	0.16
P3-21	165	11.1	BH-6	45	18.2	61	7.1
P3-21	708	3.7	BH-6	165	5.0	74	1.3
P3-21	846	2.8	BH-6	180	2.0	71	0.8

559

4 Discussion

4.1 Scalable geophysical approach for deep groundwater modeling

The integration of geophysics into groundwater studies provides an efficient and scalable substitute for borehole-based methods, especially in deep and geologically complex terrains. While boreholes provide direct *k* data, their use is limited by cost, logistics, and sparse coverage. Our study presents a robust framework for 2D and 3D *k* modeling beyond 1 km depth by integrating CSAMT with borehole data in a lithologically diverse setting. This approach addresses key challenges in areas with limited surface water and low-*k* granite near the surface, revealing deeper fractured zones with higher groundwater potential in granite, hornstone, and sandstone. These deep aquifer insights support China's national water security strategies and inform sustainable groundwater management under climate stress.

4.2 Ensuring data quality and model reliability

To minimize uncertainty and enhance accuracy, we implemented a rigorous workflow throughout data acquisition, processing, inversion, and modeling. For CSAMT, this included careful survey planning, optimized electrode configurations, and the application of advanced filtering and static shift corrections. Inversion was guided by multidimensional modeling constrained by borehole-derived a priori information, improving resolution and mitigating non-uniqueness. Permeability measurements were obtained under controlled laboratory conditions using high-quality, undisturbed core samples from six boreholes, reducing discrepancies between laboratory and field scales. These measures, together with integrated lithological data, enabled

the development of a robust *k* model suitable for reliable groundwater assessment across the study area.

4.3 Comparative advantages of CSAMT for deep hard rock aquifer characterization

CSAMT, developed in the 1970s, remains uniquely valuable for deep subsurface exploration, particularly in resistive and fractured hard rock environments. Its ability to image at intermediate-to-deep depths (hundreds to over a thousand meters) with relatively high resolution and controlled signal strength enhances its ability to delineate lithological contacts and fluid-bearing formations with precision and where other resistivity methods (VES and ERT) may fall short. While other electromagnetic methods such as MT and TDEM are also capable of probing deep subsurface structures, achieving comparable results with these methods in similarly complex hard rock settings presents notable challenges. MT, which relies on natural variations in electromagnetic fields, can reach even greater depths than CSAMT and has been successfully applied in regional-scale hydrogeological investigations, such as identifying deep groundwater circulation paths in mountain systems (Jiang et al., 2014) and tracing flow systems that recharge lowland aquifers (Gonzalez-Duque et al., 2024). However, MT's lower resolution in the upper crust and dependency on natural field conditions often limit its effectiveness in detailed, site-specific *k* modeling, particularly when borehole calibration is sparse. Similarly, TDEM is widely used for near-surface to intermediate-depth investigations and offers rapid deployment, but its signal strength and resolution tend to decrease in highly resistive formations, making it less suitable for imaging deep, fractured zones in hard rock. Therefore, while MT and TDEM are powerful methods for broad-scale groundwater assessment, they are less suited to the high-resolution, volumetric modeling of *k* in varied lithologies beyond 1km depth. In contrast, CSAMT's controlled-source design, moderate-to-deep depth penetration, and strong signal-to-

noise ratio in resistive environments make it better aligned with the goals of this study. The approach bridges the gap between large-scale geophysical surveys (e.g., MT or TDEM) and localized drilling, enabling spatially continuous 2D and 3D hydrogeophysical models essential for evaluating deep aquifer potential. While MT or TDEM may complement such studies at regional scales, achieving this level of resolution and lithological detail in a hard rock context currently remains more feasible with CSAMT.

4.4 Calibrated resistivity thresholds for lithological and hydraulic discrimination

We developed a robust empirical relationship between resistivity and *k* using 116 co-located data pairs, 62 from granite, 31 from sandstone, and 23 from hornstone, spanning 35–4,765 Ωm and 0.01–19.9 mD, respectively. The strong correlation ($R^2 = 0.96$) ensures reliable *k* prediction and minimizes lithological bias. The lithological classification derived from the resistivity–permeability relationship in this study is both geologically plausible and empirically supported by borehole data and field observations. Specifically, granite showed high resistivity (>700 Ωm) and low *k* (0–5 mD), hornstone had intermediate resistivity (350–700 Ωm) and moderate *k* (5–10 mD), and sandstone was marked by low resistivity (<350 Ωm) and higher *k* (10–20 mD). These ranges align with the distinct hydrogeological behaviors of each lithology under the site-specific structural and mineralogical conditions. The resistivity thresholds were selected through an integrated approach combining lithological logs from boreholes, established empirical resistivity values reported in the literature, and the geoelectrical contrasts identified in CSAMT profiles. For instance, the high resistivity of granite reflects its dense, low-porosity matrix and limited fluid content, whereas the lower resistivity of sandstone and hornstone corresponds to increased pore connectivity and higher saturation, often enhanced by structural features or thermal alteration. To ensure robust classification, the resistivity thresholds were calibrated using

co-located borehole observations from multiple calibration sites and iteratively refined to maximize agreement between observed lithology and the modeled resistivity–permeability domains. While we acknowledge that resistivity can vary within a given lithology due to localized factors such as fluid saturation, mineral alteration, or fracture density, sensitivity analyses indicated that moderate adjustments to the threshold values had minimal impact on the overall lithological classification or the interpretation of *k* trends. This suggests that the chosen thresholds are well-suited to the structurally complex Jinji area. Nevertheless, we emphasize that these resistivity–permeability associations are localized and should be recalibrated to account for site-specific conditions before use elsewhere. Although site-specific, the approach demonstrates how minimal calibration data can support high-resolution 2D/3D *k* modeling in data-scarce settings. Future studies could benefit from probabilistic classification schemes or machine learning approaches to further refine lithological mapping in geologically heterogeneous terrains.

4.5 Impact of lithological and measurement variability on the resistivity–permeability relationship

The fitted relationship between resistivity and *k*, as illustrated in Fig. 5, is shaped by several factors, including the geological setting, lithological heterogeneity, data distribution, and the accuracy of both measurements. The broad dynamic range in our dataset provides a strong basis for identifying trends across the three dominant lithologies: sandstone, granite, and hornstone. This broad range is especially beneficial for resolving low-*k* formations such as granite, where *k* remains uniformly low and shows minimal fluctuation. In these settings, even large shifts in resistivity translate to relatively small changes in *k*, resulting in a gently declining inverse relationship. In contrast, at lower resistivity values (e.g., <1,000 Ωm) where *k* exceeds 2 mD, small resistivity shifts result in larger changes in *k*, leading to a more scattered and nonlinear

649 correlation. This pattern is geologically realistic and reflects the inherent variability of fractured
650 and porous zones in complex lithologies.

651 **4.6 Model validation and predictive reliability**

652 Matching between measured and predicted permeability (k vs. k') was also rigorously validated
653 (Table 2). Among 18 selected points from boreholes, 10 showed a difference of less than 1 mD,
654 with only two exceeding 4 mD. Despite minor deviations, all points were accurately classified by
655 lithology. This confirms the empirical model's reliability and its utility for regional-scale k
656 prediction, even in areas lacking direct measurements. The geophysical model effectively
657 compensates for sparse drilling data, offering a scalable and cost-effective tool for
658 hydrogeological evaluation in hard rock terrains.

659 **4.7 Scale compatibility between CSAMT and permeability measurements**

660 Although pumping tests provide bulk estimates of k, they lack the spatial resolution needed for
661 detailed 2D or 3D modeling. Our goal was to capture subsurface heterogeneity, which required
662 point-specific k measurements aligned with the localized nature of geophysical-based resistivity.
663 Core data were used in lieu of pumping tests to meet the objective. The k data derived from core
664 samples at discrete depths provided a fine-scale match with CSAMT resistivity, improving the
665 accuracy of the empirical k–ρ (resistivity–permeability) relationship. The spatial resolution of
666 CSAMT ($\sim 50 \times 50$ m) closely corresponds to the scale of the core samples, ensuring
667 compatibility between datasets and supporting reliable modeling in complex geological settings.

668 **4.8 Inflection in the resistivity–permeability relationship: a depth analogue**

669 The empirical resistivity–permeability (k–ρ) relationship developed in this study exhibits a sharp
670 decline in k with increasing resistivity and a clear inflection near 1,000 Ωm. This mirrors classic
671 depth–permeability (k–z) trends (e.g., Manning and Ingebritsen, 1999; Saar and Manga, 2004;
672 Ingebritsen and Manning, 2010), where k decreases exponentially at shallow depths and follows
673 a power-law pattern deeper down. However, unlike those models that use depth alone, our
674 resistivity-based approach captures additional controls such as lithology, porosity, fluid content,
675 and fracturing, making it a more localized and physically representative proxy, especially in
676 heterogeneous hard rock settings.

677 Depth was considered but not used as the primary variable due to strong lateral variations
678 in resistivity and k caused by geological complexity. For instance, in the Jinji area, surface
679 granite shows high resistivity and low k, consistent with standard crustal profiles. However,
680 deeper hornstone and sandstone units exhibit lower resistivity and higher k, contrary to typical
681 depth trends, likely due to localized faulting, thermal alteration, and contact metamorphism that
682 enhance fracture connectivity. The resemblance between our k–ρ curve and established k–z
683 models reinforces its physical validity. The observed transition near 1,000 Ωm may reflect a shift
684 from conductive, fractured zones to compact, resistive rock masses. While hybrid models
685 incorporating depth may be useful in future work, our resistivity-based method provides a more
686 reliable and site-specific approach for k estimation in structurally complex terrains.

687 **4.9 Salinity effects and limitations of deep calibration**

688 The influence of factors beyond lithology, particularly groundwater salinity, on CSAMT-derived
689 resistivity warrants consideration. Electrical resistivity is inherently sensitive to porosity, fracture
690 density, mineral alteration, fluid saturation, and salinity. In this study, k calibration was based on

core samples from 0–200 m depths across six boreholes. While this limits direct calibration at greater depths, hydrochemical data from the Geological Survey of China, spanning 800–1,000 m depth, consistently indicate fresh groundwater, suggesting salinity is not the cause of deeper low-resistivity zones. We interpret these zones, especially in sandstone and hornstone, as reflecting high saturation and pore connectivity rather than saline fluids. This is further supported by the absence of resistivity anomalies typically associated with brackish water, and the strong alignment between resistivity, *k*, and lithological boundaries. However, due to the lack of salinity data below 1 km, the role of deep fluid conductivity cannot be fully ruled out, a limitation of the current study. Future work should include deep borehole sampling and in-situ fluid logging to better constrain this relationship.

4.10 Model construction and uncertainty in 3D permeability mapping

The 3D *k* model was developed by interpolating between 2D CSAMT inversion profiles calibrated with borehole-derived *k* from six reference locations. Due to limitations in survey geometry and computational cost, full 3D inversion was not feasible. Instead, a geostatistical framework using ordinary kriging integrated cross-sections and applied the resistivity–permeability relationship across the volume, constrained by lithological boundaries and borehole data. While this approach provides a volumetric view of *k*, model reliability declines toward the edges and corners where data density is limited. Sensitivity analyses, based on variogram adjustments and comparisons of interpolation algorithms, revealed elevated uncertainty in these peripheral zones. To convey this, uncertainty contours were added to the 3D figures (Figs. 10 and 11), delineating areas of reduced confidence. The model's core, where CSAMT lines intersect and borehole constraints exist, offers the highest reliability. Boundary regions should be

interpreted with caution. Future work with denser CSAMT coverage or full 3D inversion would enhance model accuracy and reduce edge-related uncertainties.

4.11 Limitations of storage characterization

A complete groundwater assessment requires evaluating both *k* and storage parameters. This study focused on delineating spatial variations in *k*, referred to here as "water-bearing capacity", using CSAMT-derived resistivity calibrated with borehole data. While we emphasize *k*, we acknowledge that key storage parameters such as porosity, specific yield, and specific storage remain unmeasured due to the absence of deep aquifer tests and formation logs. However, geological and geophysical evidence allows for qualitative inference. Permeable units like sandstone and hornstone likely possess higher porosity due to their granular textures and fracture networks, unlike the denser granite. This is supported by groundwater level data from six boreholes and regional water table records, which indicate aquifers in fractured, low-resistivity zones. These zones align spatially with permeable features in both CSAMT/*k* models and borehole data. Our current interpretation focuses on relative transmissivity, not absolute storage capacity, a limitation we acknowledge. Future work should include porosity and storage measurements through deep borehole testing, in-situ logging, and hydraulic analysis to support more comprehensive aquifer characterization in complex hard rock settings.

4.12 Optimizing borehole placement for CSAMT calibration

Borehole placement in this study was strategically guided by geological mapping, hydrological relevance, and preliminary geophysical data to ensure representative coverage of key lithologies and structures. These boreholes served both to calibrate resistivity–permeability relationships

and to validate the CSAMT-derived *k* models. While there's no fixed number of required boreholes, our results show that a small but well-distributed set across major lithological and structural zones yields reliable model performance. A leave-one-out validation confirmed that the model maintains coherent spatial trends, though with slightly reduced accuracy in geologically complex areas. This highlights both the importance of strategic calibration point distribution and the robustness of the CSAMT-based approach, even with limited borehole data. Future efforts could improve efficiency by adapting borehole placement based on preliminary CSAMT results, optimizing both calibration and cost.

4.13 Rationale for variable CSAMT profile extents

The variation in CSAMT profile lengths reflects site-specific logistical and geological constraints encountered during field deployment. Factors such as terrain accessibility, infrastructure (e.g., roads, buildings), and the need to capture key geological features (e.g., faults, lithological boundaries) influenced the extent of each profile. In some cases, shorter profiles were required due to rugged topography or land access limitations, while longer profiles were employed where feasible to ensure adequate coverage across broader structural domains. Despite the variation in length, all profiles were designed to achieve sufficient depth penetration and resolution for reliable resistivity–permeability modeling, as validated through borehole calibration.

4.14 Addressing the borehole–CSAMT depth discrepancy

Although the borehole data used for calibration were limited to depths of 0–200 m, this interval encompasses key lithological units, granite, hornstone, and sandstone, and captures a

representative range of resistivity and *k* conditions. These near-surface measurements provided a robust basis for developing the empirical resistivity–permeability (k–ρ) relationship, which was subsequently applied across the full depth range of the CSAMT profiles (~1300 m). While direct validation at greater depths is not currently possible due to the absence of deep borehole data, the extrapolation of the calibrated model is supported by consistent geological structure, hydrochemical data, and stratigraphic continuity reported by the Geological Survey of China down to ~1000 m. Furthermore, strong spatial alignment between resistivity, inferred *k*, and mapped lithological boundaries lends confidence to the model's deeper projections. We acknowledge this depth mismatch as a limitation, but emphasize that the approach enables meaningful *k* estimation in data-scarce regions. Future studies incorporating deep drilling and in-situ petrophysical logging will be essential to further refine model accuracy at greater depths.

4.15 Ground-truthing CSAMT with regional geological frameworks

Our results show strong agreement with regional geological and hydrogeological data from local and national surveys, confirming the reliability of the integrated CSAMT–borehole approach. This alignment supports the method's scientific validity and scalability for *k* estimation in structurally complex, data-scarce settings. While grounded in established geophysical principles, the strength of this study lies in its site-specific integration of deep *k* modeling, field validation, and empirical calibration. Overall, the findings highlight CSAMT's potential as a practical tool for deep groundwater exploration and sustainable resource management.

5 Conclusions

This study introduces a novel, non-invasive methodology for deep groundwater investigation using CSAMT, applied for indirect estimation of 2D and 3D *k* distributions in complex hard rock

terrains at depths reaching 1300 m. While borehole drilling remains the conventional means of evaluating hydraulic parameters, its high cost, limited spatial coverage, and logistical challenges restrict its broader applicability. Our approach leverages co-located CSAMT and borehole data to construct an empirical resistivity–permeability relationship, enabling the generation of spatially continuous hydrogeological models that extend beyond the reach of direct sampling.

Although the CSAMT method is inherently based on ill-posed inversion and relies on assumptions during model construction, the integration of borehole-derived ground truth allows for the calibration and partial validation of subsurface predictions. The resulting *k* models align well with regional geological features and stratigraphy. For instance, high-*k* sandstone zones (<350 Ωm, 10–20 mD) contrast distinctly with low-*k* granite zones (>700 Ωm, 0–5 mD), supporting the underlying physical relationships inferred from the data. These 2D/3D models reveal promising groundwater zones below 700 m in central regions and around granite boundaries down to 1300 m. While this study demonstrates the potential of CSAMT to enhance hydrogeological understanding in data-sparse regions, it is important to emphasize that the predictive accuracy of the models depends critically on the availability and quality of borehole data for empirical calibration.

Future work should focus on expanding the empirical dataset, integrating additional geophysical measurements, and validating models across diverse geological settings to improve generalizability. Ultimately, this combined geophysical–borehole approach holds promise for cost-effective and scalable groundwater assessment in geologically challenging environments, provided that its limitations and dependencies are clearly understood and addressed.

Code availability

Software application or custom code supports the published claims and complies with field standards

Data availability

Data available on request from the corresponding author

Author contributions

MH conceptualized the research goals and developed the methodology. MH and LS found the funding for the project. MH developed the code and prepared its visualization, and LS provided programming support and analysis tools. MH prepared the original draft.

Declaration of competing interest

The authors declare that they have no conflict of interest.

Acknowledgements

The authors gratefully acknowledge the support provided by the State Key Laboratory of Mountain Hazards and Engineering Resilience, Institute of Mountain Hazards and Environment, Chinese Academy of Sciences, and the China-Pakistan Joint Research Center on Earth Sciences, CAS-HEC, Islamabad, Pakistan.

Financial support

This research was financially supported by the National Natural Science Foundation of China (Grant No. U22A20603), the International Science and Technology Cooperation Program of Shanghai Cooperation Organization, Science and Technology Department, Xinjiang, China

(Grant No. E202301005), and the National Natural Science Foundation of China's Research Fund for International Young Scientists (RFIS-I) (Grant No. 42350410442).

References

1. Abbas, M., Deparis, J., Isch, A., Mallet, C., Jodry, C., Azaroual, M., Abbar, B., and Baltassat, J.M.: Hydrogeophysical characterization and determination of petrophysical parameters by integrating geophysical and hydrogeological data at the limestone vadose zone of the Beauce aquifer, Journal of Hydrology, 615, 128725, 2022. https://doi.org/10.1016/j.jhydrol.2022.128725.
2. Allègre, V., Brodsky, E.E., Xue, L., Nale, S.M., Parker, B.L., and Cherry, J.A.: Using earth-tide induced water pressure changes to measure in situ permeability: A comparison with long-term pumping tests, Water Resour. Res, 52(4), 3113–3126, 2016. https://doi.org/10.1002/2015WR017346.
3. Amiotte Suchet, P., Probst, J.L., and Ludwig, W.: Worldwide distribution of continental rock lithology: Implications for the atmospheric/ soil CO2 uptake by continental weathering and alkalinity river transport to the oceans, Glob Biogeochem Cycles, 17, 1038, 2003. https://doi.org/10.1029/2002GB001891.
4. Archie, G.E.: The electrical resistivity log as an aid in determining some reservoir characteristics, Transactions of the AIME, 146(1), 54–62, 1942. https://doi.org/10.2118/942054-G.
5. Asfahani, J.: Estimation of the hydraulic parameters by using an alternative vertical electrical sounding technique: case study from semiarid Khanasser valley region Northern Syria, Acta Geophys, 71, 997–1013, 2023. https://doi.org/10.1007/s11600-022-00926-0.

6. ASTM.: Standard Test Methods for Measurement of Hydraulic Conductivity of Saturated Porous Materials Using a Flexible Wall Permeameter (ASTM D5084-21), ASTM International, 2021. DOI: 10.1520/D5084-21.
7. Bauer-Gottwein, P., Gondwe, B.N., Christiansen, L., Herckenrath, D., Kgotlhang, L., and Zimmermann, S.: Hydrogeophysical exploration of three-dimensional salinity anomalies with the time domain electromagnetic method (TDEM), J. Hydrol., 380(3–4), 318–329, 2010. https://doi.org/10.1016/j.jhydrol.2009.11.007.
8. Bear, J.: Dynamics of Fluids in Porous Media. New York: American Elsevier Publishing Company, 1972.
9. Binley, A., Cassiani, G., and Deiana, R.: Hydrogeophysics: opportunities and challenges, Bollettino Di Geofisica Teorica Ed Applicata, 51(4), 267–287, 2010. [Online]. Available: http://www.scopus.com/inward/record.url?eid=2-s2.0-78650438167&partnerID=40&md5=96e14979c82f4b23e8fed0ac0140e7db.
10. Binley, A., Hubbard, S.S., Huisman, J.A., Revil, A., Robinson, D.A., Singha, K., and Slater, L.D.: The emergence of hydrogeophysics for improved understanding of subsurface processes over multiple scales, Water Resources Research, 51(6), 3837–3866, 2015. https://doi.org/10.1002/2015WR017016.
11. Borah, U.K., and Patro, P.K.: Estimation of the depth of investigation in the magnetotelluric method from the phase, Geophysics, 84 (6), E377–E385, 2019. https://doi.org/10.1190/geo2018-0124.1.
12. Brace, W.F., Walsh, J.B., and Frangos, W.T.: Permeability of granite under high pressure, Journal of Geophysical Research, 73(6), 2225–2236, 1968. https://doi.org/10.1029/JB073i006p02225.

13. Cagniard, L.: Basic theory of the magneto-telluric method of geophysical prospecting, Geophysics, 18 (3), 605–635, 1953. https://doi.org/10.1190/1.1437915.
14. Carbillet, L., Griffiths, L., Heap, M.J., Duwiquet, H., Baud, P., Violay, M.E.S., Reuschlé, T., and Guillou-Frottier, L.: The Influence of Micro- and Macrocracks on the Permeability of Granite, Rock Mech Rock Eng, 58, 1361–1378, 2024. https://doi.org/10.1007/s00603-024-04174-0.
15. Carman, P.C.: Flow of Gases through Porous Media, Academic Press, New York; Butterworths, London, 1956. 182 pp. Illus, 1956. DOI: 10.1126/science.124.3234.1254.b.
16. Chapuis, R.P., and Aubertin, M.: Predicting the Coefficient of Permeability of Soils Using the Kozeny-Carman Equation. E ´cole Polytech. Montre´al, 2003, [Online]. Available: http://publications.polymtl. ca/2605/
17. Condon, L.E., Markovich, K.H., Kelleher, C.A., McDonnell, J.J., Ferguson, G., and McIntosh, J.C.: Where Is the Bottom of a Watershed? Water Resources Research, 56(3), e2019WR026010, 2020. https://doi.org/10.1029/2019WR026010.
18. Daily, W., Ramirez, A., LaBrecque, D., and Nitao, J.: Electrical resistivity tomography of vadose water movement, Water Resources Research, 28(5), 1429–1442, 1992. https://doi.org/10.1029/91WR03087.
19. Dell'Oca, A., Guadagnini, A., and Riva, M.: Interpretation of multi-scale permeability data through an information theory perspective, Hydrol. Earth Syst. Sci., 24, 3097–3109, 2020. https://doi.org/10.5194/hess-24-3097-2020.
20. Dewandel, B., Lachassagne, P., Wyns, R., Maréchal, J.C., and Krishnamurthy, N.S.: A generalized 3-D geological and hydrogeological conceptual model of granite aquifers

controlled by single or multiphase weathering, Journal of Hydrology, 330(1–2), 260–284, 2006. https://doi.org/10.1016/j.jhydrol.2006.03.026.

21. Di, Q., Fu, C., An, Z., Wang, R., Wang, G., Wang, M., Qi, S., and Liang, P.: An application of CSAMT for detecting weak geological structures near the deeply buried long tunnel of the Shijiazhuang-Taiyuan passenger railway line in the Taihang Mountains, Engineering Geology, 268, 105517, 2020. https://doi.org/10.1016/j.enggeo.2020.105517.
22. Esmaeilpour, M., Ghanbarian, B., Sousa, R., Peter, R., and King, P.R.: Estimating Permeability and Its Scale Dependence at Pore Scale Using Renormalization Group Theory, Water Resources Research, 59 (5), e2022WR033462, 2023. https://doi.org/10.1029/2022WR033462.
23. Ferguson, G., McIntosh, J.C., Jasechko, S., Kim, J.H., Famiglietti, J.S., and McDonnell, J.J.: Groundwater deeper than 500 m contributes less than 0.1% of global river discharge, Communication Earth and Environment, 4, 48, 2023. https://doi.org/10.1038/s43247-023-00697-6.
24. Fernando, A., and Pacheco, L.: Regional groundwater flow in hard rocks, Science of the Total Environment, 506–507, 182–195, 2015. https://doi.org/10.1016/j.scitotenv.2014.11.008.
25. Ferré, T., Bentley, L., Binley, A., Linde, N., Kemna, A., Singha, K., Holliger, k., Huisman, J.A., Minsley, B.: Critical Steps for the Continuing Advancement of Hydrogeophysics. Eos, Transactions American Geophysical Union, 90(23), 200, 2009. https://doi.org/10.1029/2009EO230004.
26. Fiandaca, G., Maurya, P.K., Balbarini, N., Hördt, A., Christiansen, A.V., Foged, N., Bjerg, P.L., and Auken, E.: Permeability estimation directly from logging-while-drilling

induced polarization data, Water Resources Research, 54, 2851–2870, 2018. https://doi.org/10.1002/2017WR022411.

27. Fu, C., Di, Q., and An, Z.: Application of the CSAMT method to groundwater exploration in a metropolitan environment, Geophysics, 78 (5), B201–B209, 2013. https://doi.org/10.1190/geo2012-0533.1.

28. Fusheng, G., Haiyan, Y., Zengqian, H., Zhichun, W., Ziyu, L., Guocan, W., Linfu, X., Ye, G., and Wanpeng, Z.: Structural setting of the Zoujiashan-Julong'an region, Xiangshan volcanic basin, China, interpreted from modern CSAMT data, Ore Geology Reviews, 150, 105180, 2022. https://doi.org/10.1016/j.oregeorev.2022.105180.

29. Gerke, H.H., Dusek, J., and Vogel, T.: Mass transfer effects in 2-D dual-permeability modeling of field preferential bromide leaching with drain effluent, Hydrol. Earth Syst. Sci. Discuss., 8, 5917–5967, 2011. https://doi.org/10.5194/hessd-8-5917-2011.

30. Gleeson, T., Moosdorf, N., Hartmann, J., and van Beek, L.P.H.: A glimpse beneath earth's surface: Global hydrogeology maps (GLHYMPS) of permeability and porosity, Geophysical Research Letters, 41(11), 3891–3898, 2014. https://doi.org/10.1002/2014GL059856.

31. Glover, P.W.J.: Geophysical properties of the near surface Earth: electrical properties, Treatise on Geophysics, 11, 89–137, 2015. DOI: 10.1016/B978-0-444-53802-4.00189-5.

32. Glover, P.W.J.: What is the cementation exponent? A new interpretation, The Leading Edge, 28(1), 82–85, 2009. https://doi.org/10.1190/1.3064150.

33. Gonzalez-Duque, D., Gomez-Velez, J.D., Person, M.A., Kelley, S., Key, K., and Lucero, D.: Groundwater Circulation Within the Mountain Block: Combining Flow and Transport Models With Magnetotelluric Observations to Untangle Its Nested Nature, Water

Resources Research, 60(4), e2023WR035906, 2024. https://doi.org/10.1029/2023WR035906.

34. Hasan, M., and Shang, Y.: Geophysical evaluation of geological model uncertainty for infrastructure design and groundwater assessments, Engineering Geology, 299, 106560, 2022. https://doi.org/10.1016/j.enggeo.2022.106560.
35. Hasan, M., Shang, Y., Jin, W., and Akhter, G.: Estimation of hydraulic parameters in a hard rock aquifer using integrated surface geoelectrical method and pumping test data in southeast Guangdong China, Geosci J, 25 (2), 223–242, 2021. https://doi.org/10.1007/s12303-020-0018-7.
36. Hasan, M., Su, L., Cui, P., and Shang, Y.: Development of deep-underground engineering structures via 2D and 3D RQD prediction using non-invasive CSAMT, Scientific Reports, 15, 1403, 2025. https://doi.org/10.1038/s41598-025-85626-7.
37. Herckenrath, D., Auken, E., Christiansen, L., Behroozmand, A.A., and Bauer‐Gottwein, P.: Coupled hydrogeophysical inversion using time-lapse magnetic resonance sounding and time-lapse gravity data for hydraulic aquifer testing: Will it work in practice? Water Resources Research, 48(1), W01539, 2012. https://doi.org/10.1029/2011WR010411.
38. Herckenrath, D., Odlum, N., Nenna, V., Knight, R., Auken, E., and Bauer‐Gottwein, P.: Calibrating a Salt Water Intrusion Model with Time-Domain Electromagnetic Data, Groundwater, 51(3), 385–397, 2013. https://doi.org/10.1111/j.1745-6584.2012.00974.x.
39. Hinnell, A.C., Ferré, T.P.A., Vrugt, J.A., Huisman, J.A., Moysey, S., Rings, J., and Kowalsky, M.B.: Improved extraction of hydrologic information from geophysical data through coupled hydrogeophysical inversion, Water Resources Research, 46(4), W00D40, 2010. https://doi.org/10.1029/2008WR007060.

40. Hu, X.Y., Peng, R.H., Wu, G.J., Wang, W.P., Huo, G.P., and Han, B.: Mineral exploration using CSAMT data: application to Longmen region metallogenic belt, Guangdong Province, China, Geophysics, 78, B111–B119, 2013. https://doi.org/10.1190/geo2012-0115.1.
41. Ingebritsen, S.E., and Manning, C.E.: Permeability of the continental crust: dynamic variations inferred from seismicity and metamorphism, Geofluids, 10, 193–205, 2010. https://doi.org/10.1111/j.1468-8123.2010.00278.x.
42. ISRM.: Suggested methods for rock characterization, testing and monitoring: 2007–2014, Springer, 2015. https://doi.org/10.1007/978-3-319-07713-0.
43. Jardani, A., Revil, A., Santos, F., Fauchard, C., and Dupont, J.P.: Detection of preferential infiltration pathways in sinkholes using joint inversion of self‐potential and EM‐34 conductivity data, Geophysical Prospecting, 55(5), 749–760, 2007. https://doi.org/10.1111/j.1365-2478.2007.00638.x.
44. Jasechko, S., Seybold, H., Perrone, D., Fan, Y., Shamsudduha, M., Taylor, R.G., Fallatah, O., and Kirchner, J.W.: Rapid groundwater decline and some cases of recovery in aquifers globally, Nature, 625, 715–721, 2024. https://doi.org/10.1038/s41586-023-06879-8.
45. Jiang, X.W., Wan, L., Wang, J.Z., Yin, B.X., Fu, W.X., and Lin, C.H.: Field identification of groundwater flow systems and hydraulic traps in drainage basins using a geophysical method, Geophysical Research Letters, 41(8), 2812–2819, 2014. https://doi.org/10.1002/2014GL059579.
46. Kouadio, K.L., Liu, R., Malory, A.O., and Liu, C.: A novel approach for water reservoir mapping using controlled source audio-frequency magnetotelluric in Xingning area,

Hunan Province, China, Geophysical Prospecting, 71, 1708–1727, 2023. https://doi.org/10.1111/1365-2478.13385.

47. Laghari, A.N., Vanham, D., and Rauch, W.: The Indus basin in the framework of current and future water resources management, Hydrology and Earth System Sciences, 16 (4), 1063–1083, 2012. https://doi.org/10.5194/hess-16-1063-2012.
48. Majumdar, R.K., and Das, D.: Hydrological characterization and estimation of aquifer properties from electrical sounding data in Sagar Island region, South 24 Parganas, West Bengal, India, Asian J Earth Sci, 4, 60–74, 2011. http://dx.doi.org/10.3923/ajes.2011.60.74.
49. Manning, C.E., and Ingebritsen, S.E.: Permeability of the continental crust: Implications of geothermal data and metamorphic systems, Reviews of Geophysics, 37(1), 127–150, 1999. https://doi.org/10.1029/1998RG900002.
50. Mira Geoscience Ltd.: GOCAD Mining Suite 3D Geological Modeling Software. Nancy University, Lorraine, France, 1999.
51. Mudunuru, M.K., Cromwell, E.L.D., Wang, H., and Chen, X.: Deep learning to estimate permeability using geophysical data, Advances in Water Resources, 167, 104272, 2022. https://doi.org/10.1016/j.advwatres.2022.104272.
52. Niwas, S., and De Lima, O.A.L.: Aquifer parameter estimation from surface resistivity data, Groundwater, 41, 94–99, 2003. https://doi.org/10.1111/j.1745-6584.2003.tb02572.x.
53. Nwosu, L.I., Nwankwo, C.N., and Ekine, A.S.: Geoelectric investigation of the hydraulic properties of the aquiferous zones for evaluation of groundwater potentials in the complex geological area of imostate, Nigeria, Asian J Earth Sci, 6, 1–15, 2013. https://scialert.net/abstract/?doi=ajes.2013.1.15.

54. Pellet, H., Arfib, B., Henry, P., Touron, S., and Gassier, G.: Mesoscale permeability variations estimated from natural airflows in the decorated Cosquer Cave (southeastern France), Hydrol. Earth Syst. Sci., 28, 4035–4057, 2024. https://doi.org/10.5194/hess-28-4035-2024.
55. Phoenix Geophysics CMTPro, The Canadian Phoenix CMT Pro Version software for CSAMT data processing. Toronto, Ontario, Canada, 2020.
56. Phoenix Geophysics CSAMT-SW, The Canadian Phoenix CSAMT-SW Version software for CSAMT data inversion. Toronto, Ontario, Canada, 2020.
57. Pollock, D., and Cirpka, O.A.: Fully coupled hydrogeophysical inversion of a laboratory salt tracer experiment monitored by electrical resistivity tomography, Water Resources Research, 48(1), W01505, 2012. https://doi.org/10.1029/2011WR010779.
58. Qin, X.: Application of Unwedge program to geological stability analysis of deep buried deposits, Comprehensive, 8, 270–273, 2017 (In Chinese).
59. Revil, A., and Cathles III, L.M.: Permeability of shaly sands, Water Resources Research, 35(3), 651–662, 1999. https://doi.org/10.1029/98WR02700.
60. Rodi, W., and Mackie, R.L.: Nonlinear conjugate gradients algorithm for 2-D magnetotelluric inversion, Geophysics, 66 (1), 174–187, 2001. https://doi.org/10.1190/1.1444893.
61. Saar, M.O., and Manga, M.: Depth dependence of permeability in the Oregon Cascades inferred from hydrogeologic, thermal, seismic, and magmatic modeling constraints, Journal of Geophysical Research, 109(B4), B04204, 2004. https://doi.org/10.1029/2003JB002855

62. Simpson, F., and Bahr, K.: Practical magnetotellurics. Cambridge University Press, Cambridge. 254 pp, 2005. https://doi.org/10.1017/CBO9780511614095.

63. Singh, K.P.: Nonlinear estimation of aquifer parameters from surficial resistivity measurements, Hydrology and Earth System Sciences Discussions, 2 (3), 917–938, 2005. https://doi.org/10.5194/hessd-2-917-2005.

64. Smith, J.T., and Booker, J.R.: Rapid inversion of two-and three-dimensional magnetotelluric data, Journal of Geophysical Research: Solid Earth, 96 (B3), 3905–3922, 1991. https://doi.org/10.1029/90JB02416.

65. Soupios, P.M., Kouli, M., Vallianatos, F., Vafidis, A., and Stavroulakis, G.: Estimation of aquifer hydraulic parameters from surficial geophysical methods: a case study of Keritis Basin in Chania (Crete–Greece), J Hydrol, 1, 122–131, 2007. https://doi.org/10.1016/j.jhydrol.2007.02.028.

66. Wada, Y., Van Beek, L.P., Van Kempen, C.M., Reckman, J.W., Vasak, S., and Bierkens, M.F.: Global depletion of groundwater resources, Geophysical Research Letters, 37 (20), L20402, 2010. https://doi.org/10.1029/2010GL044571.

67. Wang, R., Yin, C., Wang, M., and Di, Q.: Laterally constrained inversion for CSAMT data interpretation, Journal of Applied Geophysics, 121, 63–70, 2015. https://doi.org/10.1016/j.jappgeo.2015.07.009.

68. Waxman, M.H., and Smits, L.J.M.: Electrical conductivities in oil-bearing shaly sands, Society of Petroleum Engineers Journal, 8(02), 107–122, 1968. https://doi.org/10.2118/1863-A.

69. Webring, M.W.: MINC: A Gridding Program Based on Minimum Curvature: U.S. Geological Survey Open File Report, 81–1224, p. 41p, 1981. https://doi.org/10.3133/ofr811224.
70. Worthington, S.R.H., Davies, G.J., and Alexander, E.C. Jr.: Enhancement of bedrock permeability by weathering, Earth-Sci Rev, 160, 188–202, 2016. https://doi.org/10.1016/j.earscirev.2016.07.002.
71. Yan, Y., Ma, L., Qian, J., Zhao, G., Fang, Y., Ma, H., and Wang, J.: Estimating permeability of rock fracture based on geometrical aperture using geoelectrical monitoring, Journal of Hydrology, 644, 132067, 2024. https://doi.org/10.1016/j.jhydrol.2024.132067.
72. Yang, J., Zhang, H., and Cui, Z.: Stability Analysis and Countermeasures of Rock Block in Underground Cavern, Guangdong Water Resources and Hydropower 5, 23–27, 2021 (In Chinese)
73. Zhang, M., Farquharson, C.G., and Liu, C.: Improved controlled source audio-frequency magnetotelluric method apparent resistivity pseudo-sections based on the frequency and frequency–spatial gradients of electromagnetic fields, Geophysical Prospecting, 69, 474–490, 2021. https://doi.org/10.1111/1365-2478.13059.
74. Zhu, L., Gong, H., Dai, Z., Guo, G., and Teatini, P.: Modeling 3-D permeability distribution in alluvial fans using facies architecture and geophysical acquisitions, Hydrol. Earth Syst. Sci., 21, 721–733, 2017. https://doi.org/10.5194/hess-21-721-2017.
75. Zonge, K.L., and Hughes, L.J.: Kenneth L. Zonge and Larry J. Hughes, (1991), "9. Controlled Source Audio-Frequency Magnetotellurics," Investigations in Geophysics, 713–810, 1991. https://doi.org/10.1190/1.9781560802686.ch9.